

## ULTRAVIOLET AND OPTICAL PROPERTIES OF NARROW-LINE SEYFERT 1 GALAXIES<sup>1</sup>

ANCA CONSTANTIN AND JOSEPH C. SHIELDS

Department of Physics and Astronomy, Ohio University, Athens, OH 45701; constant@helios.phy.ohiou.edu

To appear in *The Publications of the Astronomical Society of the Pacific*

### ABSTRACT

Narrow Line Seyfert 1 (NLS1) galaxies are remarkable for their extreme continuum and emission line properties which are not well understood. New results bearing on the spectroscopic characteristics of these objects are presented here, with the aim of establishing their typical ultraviolet (UV) and optical spectral behavior. We employ *Hubble Space Telescope* (*HST*) observations of 22 NLS1s, which represent a substantial improvement over previous work in terms of data quality and sample size. High signal-to-noise (S/N) NLS1 composite spectra are constructed, allowing accurate measurements of the continuum shape and the strengths, ratios, and widths for lines, including weak features which are barely identifiable in other Active Galactic Nuclei (AGN) composites. We find that the NLS1 sources have redder UV-blue continua than those typically measured in other quasars and Seyferts. Objects with UV line absorption show redder spectra, suggesting that dust is important in modifying the continuum shapes. The data also permit a detailed investigation of the previously proposed link between NLS1s and  $z \gtrsim 4$  quasars. Direct comparison of their composite spectra, as well as a Principal Component Analysis, suggest that high- $z$  QSOs do not show a strong preference toward NLS1 behavior.

*Subject headings:* galaxies: Seyfert—galaxies: abundances—galaxies: evolution—quasars: emission lines

### 1. INTRODUCTION

Narrow-Line Seyfert 1 galaxies (Osterbrock & Pogge 1985; Goodrich 1989) are a subclass of AGNs that manifest a distinctive ensemble of properties. They are rather rare objects that exhibit relatively narrow broad lines, strong Fe II emission, and weak emission from the narrow line region; they are more variable in X-rays than the Broad-Line Seyfert 1 objects (“normal” Seyfert 1s, hereafter Sy1), and exhibit pronounced soft X-ray excesses. They seem to cluster at one extreme end of the Boroson & Green (1992) “Eigenvector 1” (EV1) relation, as a result of their tendency toward weak [O III]  $\lambda\lambda 4959, 5007$  emission, and narrow and blue-asymmetric H $\beta$  profiles. Understanding this EV1 is important for NLS1s in particular and for AGN in general since it may be closely linked and possibly driven by the central engine parameters, in particular  $L/L_{Edd}$ , the Eddington ratio (Boroson & Green 1992; Boroson 2002). However, whether this is the main and the only physical parameter that controls the NLS1 classification, with its distinctive features, is still a matter of debate.

To date, NLS1 studies are built on either individual objects or on samples for which the spectra span only narrow wavelength ranges; also, with the exception of the X-ray observations, these samples are small in general. In particular, detailed investigations of the NLS1 blue/UV emission properties have been limited (e.g., Rodrigues-Pascual et al. 1997; Kuraszekiewicz & Wilkes 2000). Studies of their spectral energy distributions (SEDs) that cover wide bandpasses at a single epoch are almost completely missing. This kind of data is particularly useful for testing and constraining models proposed for these sources. Further examination of larger samples of NLS1 emission spectra is clearly desirable.

Understanding the nature of NLS1s requires a detailed description of their average behavior. Therefore, a first goal of the present study is to obtain a comprehensive spectral characterization of the typical NLS1 galaxy. The mounting number of high quality *HST* spectra of NLS1 sources allows for a better definition of their spectral properties in general, and their UV emission in particular. In this study, we make use of *HST* archival observations of 22 NLS1s, a sample which is nearly twice as large as any of those used in previous studies of the NLS1 ultraviolet line and continuum emission. This database includes several objects whose observations cover a wide wavelength range (Ly $\alpha$  to H $\alpha$  region) permitting thus, for the first time, a simultaneous survey of the NLS1 UV and optical spectral features. We construct average and median NLS1 composite spectra and provide measurements of the resulting underlying continuum, and the line strengths, ratios, and widths.

The second important question we attempt to address here is the degree to which NLS1s and high redshift ( $z \gtrsim 4$ ) quasars share common properties. The possible connection between these two classes of objects has been suggested by Mathur (2000), who proposed a scenario in which both NLS1s and high  $z$  QSOs are in an early evolutionary phase, such that accretion proceeds at or near the Eddington limit. This analogy is mostly based on the indications for high metallicities in both of these categories of sources, and on the presence of an enhanced low-velocity component in the UV spectra of high redshift quasars. However, no direct comparison of their emission properties has been attempted yet. This is primarily due to their wide separation in redshift, which makes it difficult to observe them in the same spectral ranges. The current availability of high-quality UV spectra for the low redshift objects al-

<sup>1</sup> Based on observations made with the NASA/ESA *Hubble Space Telescope*, obtained from the data archive at the Space Telescope Science Institute. STScI is operated by the Association of Universities for Research in Astronomy, Inc., under NASA contract NAS 5-26555.

lows us to test the validity of this picture. We examine and compare the emission properties of the NLS1s and  $z \gtrsim 4$  quasars, in order to determine the extent of the similarities exhibited by these two classes of objects. This comparison provides additional insights into AGN behavior as a function of redshift, luminosity, metallicity, and other physical parameters.

## 2. THE NLS1 SAMPLE & DATA PROCESSING

Non-proprietary, archival *HST* Faint Object Spectrograph (FOS), Goddard High Resolution Spectrograph (GHRS), and Space Telescope Imaging Spectrograph (STIS) spectra of all objects known to us that were previously identified in the literature as NLS1 galaxies (i.e.,  $\text{FWHM}(\text{H}\beta) \lesssim 2000 \text{ km s}^{-1}$ ,  $[\text{O III}]/\text{H}\beta < 3$ ), were retrieved from the Space Telescope Science Institute in the form of calibrated data. A number of these objects are borderline sources in terms of this specific classification; however, they resemble the NLS1 characteristics by every other definition, and they have been extensively used in other NLS1 studies. Table 1 summarizes the instrumental setup and the resulting total wavelength coverage corresponding to each observation. References relevant to the classification of these objects are also listed. Each line in the table refers to observations obtained under a single observing program; in all but one case (I Zw 1), these observation sets were taken at a single epoch. The data obtained under separate observing programs are listed as different lines.

In general, observations of each object were acquired with multiple gratings. The full wavelength coverage was obtained by co-adding the individual spectra, after re-sampling to a common dispersion (the lowest number of  $\text{\AA}/\text{pixel}$ , to avoid loss of information), and flux-averaging in the overlapping regions. As indicated in Table 1, there are several galaxies for which multiple observations were obtained at different epochs and in some cases with different instruments. Because these sources are characterized by significant variability, the continuum level often needed minor rescalings ( $\lesssim 10\%$ ) before averaging. The use of multiple instrumental configurations translated also into different spectral resolutions  $R$ . To obtain the final observed spectrum, it was necessary to convert the individual observations first to a common  $R$ , by gaussian smoothing of the spectra with high resolution, and second, to a common dispersion. For all objects, the averaging in the common wavelength ranges was performed by weighting the spectra by the reciprocal of their noise variance.

Many of these spectra display significant resonance line absorption. The main focus of this analysis is on the emission lines, and therefore, accurate measurements of these features required correction for the intervening absorption. When this appears as narrow lines superimposed on either the emission lines or the continuum, we removed the absorption feature through a simple interpolation. When the absorption was severe, especially near or within some of the strong emission features ( $\text{Ly}\alpha$ , N V, and C IV), a conservative reconstruction of the line was attempted by low-order polynomial fitting. For these particular cases, as indicated in Table 2, the line flux and equivalent width (EW) measurements are considered to be only lower limits.

The objects in this sample are subject to small amounts

of Galactic foreground extinction, spanning  $A_V = 0.03 - 0.31$ , with a typical value of  $\sim 0.05$  (Schlegel, Finkbeiner & Davis 1998). We corrected the spectra for the resulting reddening using the empirical selective extinction function of Cardelli, Clayton & Mathis (1989). No correction for intrinsic reddening was attempted.

In order to combine the individual source observations into a single composite spectrum, a proper alignment in wavelength of the emission lines is necessary. This requires, in turn, consistent measurements of the redshift values  $z$  used in the Doppler-correction process. Therefore, we remeasured the redshifts using the C IV  $\lambda 1549$  emission-line, which is measured in 21 out of 22 objects (the C IV feature is a doublet  $\lambda\lambda 1548.2, 1550.7$ , with the simple average of  $\lambda 1549.5$ , corresponding to the optically thick case, consistent with photoionization models). The observed wavelength for each case was established by fitting a Gaussian to the top 20% of the profile. For situations where the measured line was significantly affected by absorption or low S/N, we verified the result with fits to the top 50% of the profile. The resulting  $z$  determinations are in good agreement with previously published values, with an estimated uncertainty of  $\leq 0.001$ , and lead to a good superposition of the principal emission lines in the rest-frame. The redshift measurements obtained for each object from C IV line fitting are listed in Table 2.

Measurements of the emission features in the individual spectra were carried out with line profile fitting. This was in general unsuccessful when single Gaussians were used, as they tend to lose flux from the wings if they are prominent, and from the peak if the cores dominate. The overall shapes of the lines measured in these NLS1 spectra were generally well represented by single Lorentzian fits, which is consistent with previous findings (Moran, Halpern & Helfand 1996; Leighly 1999; Véron-Cetty, Véron & Gonçalves 2001). The C IV equivalent widths are also listed in Table 2, along with the rest-frame continuum luminosity measured at  $1450\text{\AA}$  [ $L_\nu(1450)$ , expressed in  $\text{ergs s}^{-1} \text{ Hz}^{-1}$ ]. The EW measurements may have errors resulting from the choice of continuum placement; experiments with alternative continuum fits suggest a systematic uncertainty of  $\sim 15\%$ .

Another parameter recorded in Table 2 is the spectral index  $\alpha$  of the power-law fit (defined by  $F_\nu \propto \nu^\alpha$ ) that best approximates the continuum shape of each individual object spectrum in the rest-frame. In determining the continuum solution, we tried to make use of the wavelength ranges which contain pure continuum emission. A reliable fit is obtained when a wide separation of the continuum windows is available (e.g.,  $\sim 1100 - 4000\text{\AA}$ ), such that the Fe emission, which is strong and prevalent in the UV and the blue part of the spectra of NLS1s, is avoided. In the present sample, there is only a small number of objects for which the available spectra cover completely and/or extend redward of the broad Fe II and Fe III emission-line complexes. For the sources spanning only the UV range, the measured spectral index should be considered a lower limit, as the apparent continuum can be strongly contaminated and reddened by the Fe emission. The full range of slope values and their distribution among the sample are displayed in Figure 1, along with the calculated median and average values. In identifying the Fe features, and con-

sequently the emissionless continuum windows, we used information based on high resolution spectra of I Zw1, as provided by Vestergaard & Wilkes (2001) in the UV bandpass, and by Oke & Lauer (1979) in the regions redward of Mg II  $\lambda 2797.9$ . The windows chosen in determining the power law continuum shape are placed around 1140, 1285, 1320, 1350, 1450, 3810, 3910, 4040, 4150, 5470, 5770-5800, and 6210Å, with the interval lengths ranging from 10 to 20Å. These wavelength ranges are also used in fitting the composite spectra (see Section 3.1), and they are illustrated in Figure 2.

### 3. THE NLS1 COMPOSITE SPECTRA

In this section we present NLS1 composite spectra, and resulting measurements of continuum and emission-line characteristics. The use of composite spectra is complementary to analysis of individual spectra. Composites offer higher S/N ratios, allowing measurement of weak features, while also directly providing a description of typical NLS1 spectral properties. We examine the results in relation to similar observations of broader AGN samples, in order to explore the extent to which NLS1s represent a distinct subclass. These comparisons potentially provide useful tests for discriminating between model scenarios for the NLS1 phenomenon.

#### 3.1. Overall continuum

When building spectral composites, one of the most challenging tasks is the generation of an underlying continuum that reflects the typical appearance of the sample as a whole. Francis et al. (1991) noted that “there is no ‘correct’ way of co-adding spectra that exhibit differences on many different scales.” Our sample consists only of NLS1 sources, which, as a subcategory of the AGN classification, share a set of common attributes. The spectra nonetheless show a substantial diversity in their properties. As Figure 1 and Table 2 reveal, the continuum shape, as described by the power-law index  $\alpha$ , exhibits a considerable variety among individual NLS1 spectra. Because only very few objects in the sample span the whole wavelength range, a simple median or average composite displays artificial discontinuities at locations where the number of contributing spectra changes significantly. Some care is thus required in order to use these composites to describe typical continuum properties for NLS1 galaxies.

Figure 2 presents the NLS1 average and median composites, constructed using data from individual objects normalized to the mean flux in the wavelength range 1430 Å–1470 Å. Each spectrum was given equal weight, thus avoiding biasing the resulting composites toward the brightest objects (i.e., those with the highest S/N). The median displays a smoother continuum than does the average, and is well described by a single power law ( $\alpha = -0.798 \pm 0.007$ ) from just redward of Ly $\alpha$  to H $\gamma$ . Owing to the relatively high S/N of the spectrum and the wide separation of the fitted regions, the statistical uncertainty in the spectral index, as given by a Chi-square minimization method, is

quite small. However, the value itself is rather sensitive to the precise wavelength sections employed in the fitting. Redward of H $\gamma$ , the continuum flux density rises above the level predicted by the UV power-law, and is best approximated by a separate power-law, with  $\alpha = -2.38 \pm 0.01$ . Since these objects are low-luminosity AGNs, contamination by the host galaxy starlight may contribute to this change in the spectral shape. Both fits are shown in the middle panel of Figure 2; the continuum windows used in the power-law fits are indicated as horizontal lines below the composite. Prominent emission features in the optical range are labeled. The number of objects contributing to the composites at each wavelength is presented in the bottom panel of Figure 2.

The UV-blue continuum spectral index for this *HST* NLS1 composite falls among the steepest values found in other AGN composite measurements ( $-1 < \alpha < -0.4$ ; see for example, Table 5 in Vanden Berk et al. 2001)<sup>2</sup>. Such red continua were measured only in the Zheng et al. (1997) and Telfer et al. (2002) *HST* composite spectra ( $\alpha = -0.99$ , and  $\alpha = -0.71$  respectively), and in the Schneider et al. (2001) sample of *Sloan Digital Sky Survey* very high redshift quasars (average  $\alpha = -0.93$ ). There are several possible reasons why these particular samples show such steep continua, and we explore them in the following paragraphs, in an effort to understand the origins of the extreme continuum properties of the NLS1 composites.

One effect that may contribute to the soft continuum slopes of the high  $z$  QSOs and the *HST* sources derives from the restricted wavelength baseline typically used in fitting the continua. The spectra of objects comprising these steep continuum samples make available only short regions redward of Ly $\alpha$ , in which the iron contamination may produce an artificial rise in the continuum profile (Telfer et al. 2002). However, in the NLS1 composites, the wide baseline used in fitting the continuum permits a successful accounting for the Fe II and Fe III complexes, therefore making the Fe contamination an unlikely cause for their overall red continua<sup>3</sup>.

The steepness of the *HST* composites can also potentially be attributed to an evolution of QSOs to softer spectra at lower redshifts and/or an observational bias toward detecting sources with harder continua at higher redshift (Francis 1993). The space-based observations include a significant number of low redshift sources, and this is the case for the NLS1 galaxies as well. The same evolutionary effect and the potential detection biases can also be responsible, at least partially, for the redness of the NLS1 composites, especially when compared with the ground-based composite spectra.

The present sample shows little evidence of a correlation between continuum slope and  $z$ , but a considerably stronger trend relating  $\alpha$  and luminosity (Fig. 3). Regardless of its origin, the luminosity dependence of spectral slope is probably largely responsible for the relatively steep  $\alpha$  for the NLS1 composite, since the typical luminosity of our NLS1s is lower than that of sources employed in most other quasar composites.

<sup>2</sup> Rodrigues-Pascual et al. (2000) have also reported evidence that NLS1s are redder than other Seyfert 1s at optical wavelengths.

<sup>3</sup> The Fe contamination is the primary factor that accounts for the difference between the spectral index that best fits the NLS1 median composite and the median (and average) value of the power-law index distribution of the individual continuum fits (see Figure 1). The majority of the objects in the NLS1 sample cover only the UV wavelength region, where the power-law solution is unable to properly estimate the true underlying level below the Fe II and Fe III emissions, and as a consequence, steeper indices are measured.

### 3.2. Reddening and Absorption

The luminosity dependence of spectral slope could be intrinsic to the accretion source, but independent evidence suggests that it is mostly attributable to luminosity-dependent reddening. Internal dust, if present, is expected to be accompanied by gas producing observable absorption lines. In our sample, the signature of strong absorption near the systemic velocity of the host galaxy is present in almost half the objects (see Table 2). Median values of the spectral indices corresponding to subsamples of sources with and without strong resonance line absorption are  $-1.34$  and  $-0.73$  respectively, consistent with steeper (redder) continua in the absorbed NLS1s. Median logarithmic luminosity values for the absorbed and unabsorbed subsamples are  $29.01$  and  $29.60$  respectively (mean values are  $28.4 \pm 0.4$  and  $29.3 \pm 0.2$  respectively), thus directly linking the presence of absorption with luminosity.

The location and physical state of the absorbers in NLS1s may be important for understanding these objects. Intrinsic absorption related to the central accretion source is now known to be present in a significant fraction of Seyfert 1 nuclei (Crenshaw et al. 1999). NLS1s exhibit similarities in emission properties to low-ionization broad absorption-line QSOs (BALQSOs), which Boroson (2002) has interpreted as evidence for high luminosities relative to the Eddington value for both classes of object; in the BALQSOs, the absorption is clearly also closely related to the accretion process. In the NLS1s, the intervening gas may be a warm (highly ionized) absorber that is potentially dusty (e.g., Komossa & Greiner 1999); alternatively the absorbing matter may be related to the “lukewarm absorber” identified in case studies by Kraemer et al. (2000) and Crenshaw et al. (2002), which may reside on kpc scales. The luminosity dependence of reddening and absorption for the NLS1s is consistent with a scenario in which the absorbing matter covers a larger solid angle as seen by the central source in lower luminosity objects, a natural expectation for interstellar matter in a disk-like geometry of luminosity-independent scale-height, but with a sublimation radius for dust that scales with luminosity, similar to the ‘receding torus’ model (Lawrence 1991). If the absorbing medium has a flattened distribution aligned with the host galaxy disk, we might then expect a correlation between the host inclination and the spectral (UV) color, as reported for several Seyfert 1s by Crenshaw & Kraemer (2001). Inclination values are available in the literature for 16 of our sample members; the data do not show a statistically significant trend with  $\alpha$ , however. In summary, the extent to which the UV/optical absorbers in NLS1 nuclei are associated with the central accretion structure versus the normal host galaxy interstellar medium remains ambiguous.

The nature of the dusty absorber in these galaxies can be further tested by analyzing their soft X-ray ( $0.1 - 2.4$  keV) characteristics. A “lukewarm” (low ionization) constitution of the gas would suggest strong absorption, that translates into flatter observed soft X-ray spectra. If a “warm” (high ionization) absorber is present, steeper X-ray continua should be measured (Grupe et al. 1998). The *ROSAT* spectral indices ( $\Gamma \equiv 1 - \alpha$ ) are available for the majority of the NLS1s employed in this study, and are recorded in Table 2. Splitting the sample into absorbed

and unabsorbed objects, as before, and calculating the median value of the X-ray spectral slope for each subgroup, should provide us a rough criterion for distinguishing between the two types of absorbers. The resulting values are  $\Gamma_{\text{absorbed spectra}} = 3.4$  and  $\Gamma_{\text{unabsorbed spectra}} = 3.1$ , nominally implicating the presence of highly ionized absorbers (mean values are  $4.2 \pm 0.8$  and  $3.3 \pm 0.2$  respectively); however, the difference in the median values is small, and it appears likely that the absorbing medium in these objects is described by a range of properties.

### 3.3. The UV spectrum

Figure 4 shows the average spectrum in the UV range, where most of the objects ( $\geq 18$ ) in the sample are contributing. The standard deviation (RMS) and the standard deviation of the mean spectra show the degree of variation between the members of the sample and the uncertainty of the average composite as a function of wavelength. Near the wavelength corresponding to the common continuum normalization ( $\lambda \sim 1450\text{\AA}$ ), the spectral variation within the NLS1 sample is dominated by the modulations in the cores of the strongest emission lines (Ly $\alpha$ , C IV, He II, and C III]). In this respect, NLS1s behave like the other more general samples of AGNs (e.g., Francis et al. 1992; Brotherton et al. 2001). Away from the normalization wavelength interval, the bulk of the spectral variance is accounted for by differences in the individual continuum shapes and noise.

### 3.4. The optical composite

For wavelengths  $\lambda \gtrsim 3000\text{\AA}$ , the *HST* NLS1 spectrum is based on only a small number of objects. Because fewer than 5 NLS1s make up the composites at these wavelengths, the individual source contributions are more pronounced, making it difficult to identify and measure the spectral features (continuum and emission lines) located at the transition points in the number of contributing objects (e.g., at  $\sim 4360\text{\AA}$ ,  $\sim 5500\text{\AA}$ ). A smoother spectrum is constructed using only the three spectra that span the whole wavelength range (Ark564, Mrk493, WPVS007), and is presented in Figure 5. We compare our optical median composite with the Sulentic et al. (2002) median NLS1 spectrum, constructed from a much bigger sample (24 sources, ground-based spectra). The two spectra are very similar in both the continuum shape and the profile and strength of emission features. Small differences, like the stronger peaks in the emission lines in the *HST* composite, are mostly due to the different spectral resolution that characterizes the two samples ( $4 - 7\text{\AA}$  FWHM for the Sulentic spectra,  $\sim 2\text{\AA}$  for the *FOS-HST* observations). The good agreement between the two medians suggests that the *HST* composites are representative of typical NLS1 optical spectra, despite the fact that they are constructed from such a small object sample.

### 3.5. Emission Lines

The richness of the line emission in the AGN spectra is easily distinguishable in the NLS1s due to their narrow widths. Hence, careful identification and intensive analysis of the NLS1 emission lines have been performed, though to date, only on individual sources, e.g. I Zw1 (Laor et al. 1997; Vestergaard & Wilkes 2001, and references

therein). When composites are built using relatively large samples, higher S/N is achieved, and therefore, higher accuracy is expected in identifying and measuring the emission lines. We have been able to detect and parametrize in the *HST* NLS1 composites a large number of emission features. Many are barely present or are heavily blended, and therefore difficult to quantify in other AGN composites (Francis et al. 1991; Vanden Berk et al. 2001; Zheng et al. 1997; Telfer et al. 2002).

The emission lines are measured from the average composite, as it presents a higher S/N ratio than the median spectrum. An exception is made for the wavelength interval  $\sim 2900 - 3170 \text{ \AA}$ , where the emission features in the average spectrum are distorted by the jumps present in the continuum shape (see Section 3.1), and where the median is used. Line fluxes, strengths (EWs), widths (FWHM) and line shifts relative to the laboratory central wavelengths ( $\Delta v$ ) are listed for all detected features, along with their  $1 \sigma$  error bars, in Table 3. The lines have been identified by matching wavelength positions and respective relative strengths of features found in the Francis et al. (1991), Zheng et al. (1997), Vanden Berk et al. (2001) and Telfer et al. (2002) composites, and in the detailed analyses of I Zw1 (Laor et al. 1997; Vestergaard & Wilkes 2001). Tentative identification of newly discovered features is based mainly on data available from the Atomic Line List<sup>4</sup> and Verner et al. (1996).

All measurements, including the peak positions of each emission line,  $\lambda_{mean\_rest}$ , and the respective errors are generated using the task *specfit* (Kriss 1994) as implemented in the IRAF<sup>5</sup> software package. The method employs line and continuum spectral fitting via an interactive  $\chi^2$  minimization. The fit is performed in 14 separate spectral intervals; their lengths varied, in order to keep a reasonable number of parameters, from  $\sim 150 \text{ \AA}$  in the UV-blue region, rich in prominent emission features, to  $\sim 500 - 900 \text{ \AA}$  in the optical range. The equivalent widths are measured relative to the resulting local continua, which differ from the shape estimated in Section 3.1, mainly due to the fact that the average and not the median composite is used in the fitting process. Comparisons indicate that line fluxes measured in the average and median composites are consistent to within  $\lesssim 10\%$  in most cases.

For most features, the line emission is modeled using single Lorentzian profiles. However, the most prominent lines required two components, a narrow and a broad Lorentzian, the broad one being in general blueshifted relative to the narrow component. The broad and prominent Fe emission surrounding and redward of Mg II  $\lambda 2798$  is not measured; thus, line measurements for  $2000 \text{ \AA} \lesssim \lambda \lesssim 4250 \text{ \AA}$  may include some Fe contamination, and therefore, a high level of uncertainty. For the optical wavelength range, redward of  $H\gamma$ , we use in the fitting process the empirical Fe II template obtained by Boroson & Green (1992) from the I Zw1 spectrum. No broadening of the iron template was necessary in order to match the line

width of the NLS1 composite spectra. In fitting forbidden line doublets, the line pairs are assigned to have common velocity widths and offsets, and their flux ratios are constrained to values determined by branching ratios, when appropriate.

Because the composites were constructed using redshifts based on the position of a single emission-line, C IV (see Section 2), a check for systematic velocity offsets for other lines can be performed. Such line shifts, which are definitely present for many of the lines listed in Table 3, have been detected previously in other AGN samples (e.g., Gaskell 1982; Espey et al. 1989; Tytler & Fan 1992; McIntosh et al. 1999; Vanden Berk et al. 2001). Note that most of the lines are redshifted relative to C IV, the reference line, and that the largest values of the recorded velocity shifts correspond to the lowest ionization states (e.g., Si II, C II, O I). Figure 6 shows the velocity shifts versus the ionization potentials, compiled for all emission lines that are stronger than C II  $\lambda 1335$ , i.e.,  $EW \gtrsim 4.0 \text{ \AA}$ , and that have well defined non-blended peaks. We treat the permitted and the forbidden lines separately since they may have very different origins. The values for the ionization potentials are chosen such that, for the recombination lines of H and He, they express the energy necessary to ionize the respective state for later recombination, while for the collisionally excited lines from heavy elements, they represent the energy that is needed to create the ionization state. For the most prominent features, which are fitted with two components, we consider only the velocity shift measurements given by their narrow components (they are identified by different symbols in Figure 6, upper panel); this treatment is justified by the fact that the reference wavelength is chosen based on the location of the peak of C IV, which is measured using the narrow component fit<sup>6</sup>. This approach is consistent with measurements of velocity offsets performed in previous similar studies of other AGN samples (e.g. Vanden Berk et al. 2001).

The results presented in Figure 6 provide evidence for an anticorrelation between the velocity shifts and the degree of ionization of the emitting species. The trend is definitely present in both categories of emission features. For the forbidden lines, significant velocity shifts, usually blueshifts relative to the systemic velocity, have been detected in the past for the high ionization transitions (e.g., Penston et al. 1984; Appenzeller & Wagner 1991); however, the evidence for a correlation similar to that presented in this study has only recently been revealed by measurements from the high S/N *Sloan Digital Sky Survey* quasar composite spectrum (Vanden Berk et al. 2001). In both types of lines measured in the NLS1 sources, the amplitude of this correlation appears similar to that present in other, more heterogeneous Sy1/quasar samples<sup>7</sup>. Although the ionization potential seems to govern the magnitudes of the velocity offsets, there is a significant amount of scatter in this empirical relationship, in both Sy1/quasars

<sup>4</sup> The Atomic Line List is hosted by the Department of Physics and Astronomy at the University of Kentucky; <http://www.pa.uky.edu/~peter/atomic>.

<sup>5</sup> The Image Reduction and Analysis Facility (IRAF) is distributed by the National Optical Astronomy Observatories, which is operated by the Association of Universities for Research in Astronomy Inc. (AURA), under cooperative agreement with the National Science Foundation.

<sup>6</sup> Single Lorentzian fits for these features result in line shifts that differ by  $\lesssim 100 \text{ km s}^{-1}$  from the ones given by the narrow component only; this is due to the fact that the cores of these relatively narrow lines account for the bulk of the flux.

<sup>7</sup> The velocity shifts may be unusually large in I Zw 1; see Laor (2000).

and NLS1 objects, suggesting the influence of other parameters as well. The scatter in the NLS1 trend may be amplified by wavelength zero-point calibration uncertainties, particularly for the FOS spectra.

The origin of the velocity offsets between the AGN emission lines is not well understood, but a promising means of interpreting this behavior is in terms of the disk-wind model for the broad-line region (BLR). In this picture, the high ionization lines are produced in outflowing winds, accelerated by radiative line driving, that arise from the accretion disk, which is the base for the low-ionization emission (e.g., Murray & Chiang 1998; Proga, Stone & Kallman 2000; Leighly 2001). Additionally, the disk and/or the radiative outflow itself, believed to proceed from near the plane of the disk, is assumed to be optically thick, so the emission from the receding wind is obscured.

The fact that NLS1s and other broad-line AGNs show similar line shifts provides additional constraints for the physical models that best characterize the NLS1s. The preferred explanations for the primary drivers of the NLS1's extreme measured properties postulate either higher ratios of their luminosity to the Eddington luminosity (e.g., Pounds et al. 1995), or a more pole-on view of an assumed disk-shaped BLR (e.g., Brandt & Gallagher 2000). The velocity offsets between lines reported here, and their similarity to those found in less restricted AGN samples, may present a challenge to either NLS1 scenario, if the velocity differences stem from a disk-wind phenomenon or something similar. For the orientation model, it would be surprising if the typical line-of-sight *differences* in line velocity remain essentially unchanged when the orientation is such that the line *widths* are diminished. For the high Eddington ratio picture, the offsets ultimately trace the disk outflow velocity, which is expected to scale with the local orbital speed, hence large velocity differences combined with small widths are again unexpected. The solution in either case may ultimately involve the fact that the narrow line widths characterize only a subset of emission features in NLS1s, notably including the  $H\beta$  feature, while other lines (particularly in the UV) still reveal high-velocity gas components. Indeed, as discussed by Wills et al. (2000), and elaborated by Shang et al. (2003), the UV line widths do not correlate in a simple way with  $H\beta$  width or with other NLS1 defining properties.

#### 4. ARE NLS1S THE ANALOGUES OF HIGH $z$ QSOs?

Based on the apparent similarity of some of the emission properties of NLS1s and  $z \gtrsim 4$  QSOs, Mathur (2000) suggested a connection between these two classes of AGNs, in the sense that the NLS1s are the low redshift, low luminosity analogues of the high  $z$  quasars. In the proposed picture, both categories of sources are in an early evolutionary phase, in which accretion proceeds at or near the Eddington limit. This scenario has several appealing aspects for explaining NLS1 phenomena, but additional tests are desirable to verify this idea, and especially to gauge its applicability to the high  $z$  sources.

One of the key arguments employed in support of a NLS1 – high  $z$  QSO association was the initial report of narrow UV lines in  $z \gtrsim 4$  quasars by Shields & Hamann (1997). While the presence of an enhanced low-velocity

component in the high redshift quasars was later confirmed by Constantin et al. (2002), the UV line profiles do not necessarily provide an adequate basis for linking the high  $z$  QSOs to a NLS1 classification, as this is based on optical lines. In fact, as noted above (Section 3.5), the UV and optical emission-line properties are substantially independent (Shang et al. 2003).

Another possible similarity between high  $z$  quasars and NLS1 galaxies is a high metallicity ( $Z$ ) in their emitting gas. In quasars at  $z \gtrsim 3$ , super-solar heavy element enrichments have been derived in specific abundance studies based on both emission (Dietrich et al. 1999; Dietrich & Wilhelm-Erkens 2000; Dietrich et al. 2003) and absorption properties (e.g., Hamann 1997). The high gas-phase metallicity is believed to derive from a recent episode of vigorous star formation. For the NLS1s, several lines of argument have suggested the presence of enhanced metallicity. One of the potential indicators of high abundances in these objects is their characteristically strong Fe II emission (Collin & Joly 2000). However, the excitation of this emission is complicated and its strength does not necessarily map in a simple way to the Fe abundance (e.g., Verner et al. 1999). Moreover, if the Fe is largely produced in Type-Ia supernovae, as would be expected, the evolution of the progenitor population and the resulting enrichment should occur on a timescale  $\gtrsim 1$ Gyr; consequently, a high iron enrichment is not a strong indicator of youth, and therefore, would not support the hypothesis of NLS1s being galaxies in the making.

A better tracer of abundances in NLS1 galaxies is provided by nitrogen. This element is of particular interest since its production is believed to be dominated by secondary enrichment, which translates into  $N/H \propto Z^2$ . Nagao et al. (2002) have recently discussed the forbidden line spectra of NLS1s, including [N II]  $\lambda 6583$ , and argued that the observed line ratios suggest higher metallicities than in the Sy1s; as the authors also point out, however, this statement is very model-dependent. More robust diagnostics are obtained from studies of the N V  $\lambda 1240$  feature, and in particular, measurements of its strength relative to C IV  $\lambda 1549$  and He II  $\lambda 1640$  (Hamann et al. 2002, and references therein). Evidence for systematic trends of stronger N V and weaker C IV with increasing EV1 (which seems to trace NLS1 behavior, see Section 1) has been reported by Wills et al. (1999). Based on the same flux ratios, Shemmer & Netzer (2002) showed that the NLS1 sources deviate significantly from the well known relationship between  $Z$  and luminosity ( $L$ ) in AGNs (Hamann & Ferland 1993), by exhibiting higher  $Z$  at a given  $L$ . Interestingly, several of the nine extreme NLS1s used in their study have line ratios as high as those measured in the most luminous high  $z$  QSOs. Measurements for larger samples of NLS1s are clearly desirable to verify these findings.

In this section, we investigate the NLS1 –  $z \gtrsim 4$  QSO analogy by directly comparing their emission-line properties. As most of the line emission studies of the NLS1 objects are in the optical regions, and the corresponding (rest-frame) data for  $z \gtrsim 4$  are almost nonexistent, the UV spectral observations are the only accessible tool to exploit in such a comparison. We have available both NLS1s and high  $z$  quasar UV data, for samples that permit an adequate statistical analysis of their emission characteris-

tics. Our study employs both comparisons of their composite spectra, and an eigenvector analysis that determines the degree to which the spectral variances throughout the samples share common properties. The NLS1 objects and composites used here are described in Sections 2 and 3.1. For the  $z \gtrsim 4$  QSO sample, we made use of 44 spectra of non-BAL quasars, presented by Constantin et al. (2002) and Schneider, Schmidt & Gunn (1991), which span the 1100 – 1700Å rest-frame range.

#### 4.1. Direct comparison of composite spectra

Figure 7 shows the NLS1 average composite (Section 3.1) overplotted on the  $z \gtrsim 4$  QSO average composite (Constantin et al. 2002). In a first approximation, the spectra agree well: similar continuum shape and the same strong emission lines, with comparable profiles. The pronounced Ly $\alpha$  forest in the  $z \gtrsim 4$  composites does not reflect an intrinsic difference in the nature of the emission sources, but the expected increase in the opacity of the intergalactic medium at larger redshifts.

The most evident distinction between the NLS1 and high  $z$  quasar composite spectra is in the strength of the principal emission features: Ly $\alpha$ , Si IV+O IV], C IV and He II. This difference in the line strengths is a clear manifestation of the Baldwin Effect (the inverse equivalent width – luminosity relationship, Baldwin 1977). The two samples differ significantly in their average luminosity, with the lower luminosity objects, the NLS1s, exhibiting stronger lines. Figure 8 shows the individual measurements of the rest-frame continuum luminosity,  $L_\nu(1450\text{\AA})$ , and the strength (EW) of the C IV line, plotted for both the NLS1s and high  $z$  quasars. The Baldwin Effect correlation in C IV is clearly present over the combined sample; the segregation in luminosity of the two samples is also evident<sup>8</sup>. Besides the basic Baldwin trend, the comparison in Figure 7 shows also the known trend with ionization: steeper Baldwin Effect for more highly ionized species (e.g., Dietrich et al. 2002). The difference in the strength of the emission lines in the NLS1 and high  $z$  QSO composites is likewise most obvious in Ly $\alpha$  and the high ionization features (Si IV+O IV], C IV and He II), and almost absent in the low ionization lines (O I, C II). As found in previous studies of the Baldwin relationships, the N V $\lambda$ 1240 emission proves to be the exception for which the line strength remains nearly independent of luminosity.

Another important issue that can be examined via comparison of the composite spectra is the degree of similarity in the chemical enrichment for the two source types. As noted before, the broad line region enrichments in both  $z \gtrsim 4$  QSOs and NLS1s have been evaluated based on the N V/C IV and N V/He II line ratios, as best indicators of the overall metallicity. Figure 7 shows that the N V emission feature is equally strong in the NLS1 and high  $z$  QSO average composites. Deblended measurements of this line obtained from detailed fits of the Ly $\alpha$ +N V+Si II\*+Si II emission-line complex confirm this result. C IV and He II are however much stronger in the NLS1 spectra than in those of the  $z \gtrsim 4$  QSOs<sup>9</sup>. These trends result in lower N V/C IV and N V/He II line ratios, and presumably lower

average metallicities, in the NLS1 sources than in the high  $z$  quasars, and thus do not support a strong connection between the two classes of objects. The results of this comparison differ from those of Shemmer & Netzer (2002) who argued that the line strengths suggest comparable metallicity for the NLS1s and the high luminosity QSOs. However, their conclusion was based on a very small number of NLS1s; also, the high abundances in these sources were supported by a relatively large N V/C IV ratio, but not clearly confirmed by N V/He II. The discrepancy between their findings and ours may be related to the details of the samples used in each case. With the larger sample size employed here, we tentatively conclude that the abundances in NLS1s and high  $z$  QSOs are in fact characteristically different; further study with larger sets of object spectra would clearly be desirable.

#### 4.2. Principal Component Analysis

Additional information on the NLS1 –  $z \gtrsim 4$  QSO relationship can be obtained by the means of a Principal Component Analysis (PCA), a mathematical decomposition of a set of properties describing the sample into a smaller number of eigenvectors that can account for the bulk of the total variance present in the data. Due to the fact that quantitative measurements of the spectral properties are in general subjective to the chosen parametrization, we chose to apply the PCA method directly to the observed spectra (e.g., Francis et al. 1992). We proceed with this analysis for the two samples separately, and for the combined set as well. This approach should allow for further identification of potential common behaviors and their distribution among the two object classes.

For the NLS1 data, the spectral range with the most extensive coverage among the sample objects (21 out of 22) spans the region around the C IV line, and this bandpass is thus optimal for detailed statistical investigation. In this wavelength range, the  $z \gtrsim 4$  QSO sample is well represented by all 44 object spectra. Therefore, we conduct the PC analysis on this interval, where the highest S/N is expected. Figure 9 shows the mean spectra, the RMS spectra, and the first five principal components (PCs), ordered by the fraction of the sample variance for which each accounts, for the NLS1s, high  $z$  QSOs, and the combined sample. The *range* of properties exhibited by these objects is illustrated by the PCs and by their contribution to the total spectral variation. Principal Component 1 (PC1) is dominated by line-core modulations (compared with the emission in the average composites), and therefore, it can be considered primarily as a measure of the strength of the lines. This is a similar result to what Francis et al. (1992) obtained with PC analysis for a larger and more heterogeneous sample (232 objects), from the Large Bright Quasar Survey (LBQS). Aside from a scale factor, this first principal component is very similar for the three samples. Its profile differs in the two individual samples ( $\text{FWHM}(\text{NLS1s}) = 2050 \text{ km s}^{-1}$ ,  $\text{FWHM}(z \gtrsim 4 \text{ QSOs}) = 3100 \text{ km s}^{-1}$ ); as might be expected, the NLS1 core contribution is narrower than that in the high  $z$  QSOs. The second component, PC2, accounts for spectrum-to-spectrum

<sup>8</sup> The flattening of the Baldwin correlation at low luminosities has been reported in several previous studies; see Osmer & Shields (1999) for discussion and references.

<sup>9</sup> The same results are obtained when median composites are used for comparison.

variations present in the wings of the lines. This is again exhibited by both samples but in a much larger proportion by the NLS1s. Also, the line-core and the line-wing modulations show opposite trends, suggesting that objects with prominent wings possess weak cores. Higher-order components continue to display, in different proportions, the core and the wing variations, but their intricacies become difficult to characterize and compare.

Associating physical explanations to the properties exhibited by PCs is difficult, but additional information can be gained from the statistics of the PCA results. Table 4 lists the proportions (fractions of total variance) contributed by the first five PCs for each individual sample and for the combined one. The numbers indicate that the NLS1 sample can be better represented than the  $z \gtrsim 4$  quasar sample by a low number of principal eigenvectors. The difference in the PCs' individual and cumulative proportions indicate that NLS1 sources comprise a more spectroscopically compact sample than the high  $z$  quasars. Another basis for evaluating these results is a statistical comparison of the distributions of the weights of the first two principal components for the NLS1 and  $z \gtrsim 4$  QSO objects. In the PCA run for the combined sample, i.e., for a common set of eigenvectors representing the NLS1s and the high  $z$  QSOs, the Kolmogorov-Smirnov (KS) test shows that the possibility of the two data sets being drawn from the same parent population is not excluded, but the evidence for this is weak: the KS probabilities are 0.047 and 0.188 for weights of PC1 and PC2 respectively.

As a consistency test, we also performed this analysis for a much larger spectral range, covering Ly $\alpha$  to He II bandwidth, but with a lower number of NLS1s (only 16 objects), and therefore lower statistics; the main results remained unchanged. NLS1s and  $z \gtrsim 4$  QSOs are probably not close spectroscopic or physical analogues.

## 5. CONCLUSIONS

In this paper we present an analysis of all publicly available spectra for NLS1 galaxies in the *HST* archive. The resulting sample of 22 NLS1s with spectra spanning the UV-blue wavelength range is the largest that has been used, to date, in emission line studies of these objects. We employed these data to construct composite spectra (average and median), and thus, to characterize in detail the typical spectral properties of the NLS1 class.

The resulting composite spectra are used to estimate the strengths of a large number of emission lines, and to quantify the continuum shape over a broad bandpass. Power-law fits to the continuum indicate a discrepancy from the results obtained from more general AGN composite studies: NLS1s have steeper UV-blue spectra. Possible explanations include intrinsic reddening and a trend of the low redshift sources to have intrinsically softer continua. A relation between the continuum shape and the redshift is not readily evident in this sample. A significant correlation is however observed between the spectral slope and luminosity, indicating that the redness of the NLS1s is related to the low luminosity of these objects. More-

over, the apparent connection between the UV resonance absorption lines and luminosity suggests that the steep slopes measured in these objects are due at least partially to reddening. The ionization state of the absorbing material and its relationship to the accretion source are not well determined, however.

The NLS1 composites additionally allow us to quantify emission-line velocity offsets. The correlation between the velocity shifts and the degree of ionization that is found in normal broad-line AGNs is also present in the NLS1 sources, in both permitted and forbidden lines. This result may be of interest for comparison with NLS1 model predictions.

The NLS1 data permit further investigation into the proposed analogy between these sources and the  $z \gtrsim 4$  quasars. Previous work suggested that both may be described by a high accretion rate and super-solar metallicities. The comparative study that we conduct based on the NLS1 and high  $z$  quasar average UV emission properties reveals a significant contrast between their spectral characteristics. The composite spectra exhibit primarily the anticipated differences associated with the Baldwin Effect, i.e., relatively stronger lines in the less luminous sources. Nonetheless, the comparison makes it evident that the metal enrichment of the surrounding gas in the high  $z$  QSOs is higher than that in the NLS1 objects. This result does not support the hypothesis that these two types of objects are similar in their detailed physical characteristics or evolutionary phase.

Additional confirmation of the differences exhibited by the two types of objects comes from a principal component decomposition applied directly to the spectra. The spectral PC analysis indicates that the  $z \gtrsim 4$  sources are statistically likely to share only part of their emission properties with the NLS1 galaxies; in particular, the low-velocity component, although enhanced in the high  $z$  QSOs, is less prominent than in the NLS1 objects. The statistics show that the  $z \gtrsim 4$  QSO phenomenon is controlled by a broader, more heterogeneous family of properties than those governing the NLS1s; the NLS1 spectroscopic features can be reconstructed from a smaller number of parameters (eigenvectors) than that necessary in the case of  $z \gtrsim 4$  sources. In conclusion, NLS1s and high  $z$  quasars are spectroscopically disparate, and it is therefore doubtful that a close physical connection exists between these source types.

The authors thank Todd Boroson for providing the I Zw1 Fe template spectrum in digital form, Don Schneider for the high  $z$  QSO spectra in digital form, Paul Francis for access to his PCA software, and Fred Hamann for helpful discussions. We also gratefully acknowledge Ari Laor and the anonymous referee for providing comments on the original manuscript that resulted in improvements. Support for this research was provided by NASA through grant GO-09143.02 from the Space Telescope Science Institute, which is operated by the Association of Universities for Research in Astronomy, Inc., under NASA contract NAS5-26555.



## REFERENCES

- Appenzeller, I. & Wagner, S. J., 1991, *A&A*, 250, 57  
 Baldwin, J.A. 1977, *ApJ*, 214, 769  
 Boller, Th., Truemper, J., Molendi, S., Fink, H., Schaeidt, S., Caulet, A., & Dennefeld, M., 1993, *A&A*, 279, 53  
 Boller, Th., Brandt, W. N., & Fink, H., 1996, *A&A*, 305, 53  
 Boroson, T. A. & Green, R. F., 1992, *ApJS*, 80, 109  
 Boroson, T. A., 2002, *ApJ*, 565, 78  
 Brandt, W. N., & Gallagher S. C., 2000, *NewA Rev.*, 44, 461  
 Brotherton, M. S., Tran, H. D., Becker, R. H., Gregg, M. D., Laurent-Muehleisen, S. A., & White, R. L. 2001, *ApJ*, 546, 775  
 Cardelli, J. A., Clayton, G. C., & Mathis, J. S. 1989, *ApJ*, 345, 245  
 Collin, S. & Joly, M., 2000, *NewA Rev.*, 44, 531  
 Constantin, A., Shields, J. C., Hamann, F., Foltz, G. B., & Chaffee, F. H., 2002, *ApJ*, 565, 50  
 Crenshaw, D. M., Kraemer, S. B., Boggess, A., Maran, S. P., Mushotzky, R. F., & Wu, C., 1999, *ApJ*, 516, 750  
 Crenshaw, D. M. & Kraemer, S. B., 2001, *ApJ*, 562, 29  
 Crenshaw, D. M., et al., 2002, *ApJ*, 566, 187  
 Dietrich, M., et al., 1999, *A&A*, 352, L1  
 Dietrich, M., & Wilhelm-Erkens, U., 2000, *A&A*, 354, 17  
 Dietrich, M., Hamann, F., Shields, J. C., Constantin, A., Junkkarinen, V. T., Chaffee, F. H., 2002, & Foltz, G. B., 2002, *ApJ*, in press  
 Dietrich, M., et al. 2003, in preparation  
 Espey, B. R., Carswell, R. F., Bailey, J. A., Smith, M. G., & Ward, M. J. 1989, *ApJ*, 342, 666  
 Francis, P. J., Hewett, P. C., Foltz, C. B., Chaffee, F. H., Weymann, R. J., & Morris, S. L. 1991, *ApJ*, 373, 465  
 Francis, P. J., Hewett, P. C., Foltz, C. B., & Chaffee, F. H. 1992, *ApJ*, 398, 476  
 Francis, P. J. 1993, *ApJ*, 407, 519  
 Gaskell, C. M. 1982, *ApJ*, 263, 79  
 Goodrich, R. W., 1989, *ApJ*, 342, 224  
 Grupe, D., Beuermann, K., Mannheim, K., & Thomas, H.-C., 1998, *A&A*, 350, 805  
 Grupe, D., Beuermann, K., Thomas, H.-C., Mannheim, K., & Fink, H. H., 1999, *A&A*, 330, 25  
 Hamann, F., & Ferland, G., 1993, *ApJ*, 418, 11  
 Hamann, F., 1997, *ApJS*, 109, 279  
 Hamann, F., Korista, K. T., Ferland, G. J., Warner, G., & Baldwin, J., 2002, *ApJ*, 564, 592  
 Komossa, S., & Greiner, J., 1999, in *ASP Conf. Ser. 161, High Energy Processes in Accreting Black Holes*, ed. J. Poutanen & R. Svensson (San Francisco: ASP), 228  
 Kraemer, S. B., George, I. M., Turner, T. J., & Crenshaw, D. M., 2000, *ApJ*, 535, 53  
 Kriss G., 1994, in *ASP Conf. Ser. 61, Astronomical Data Analysis Software and Systems III*, ed. Crabtree, D. R., Hanisch, R.J., & Barnes, J., 437  
 Kuraszekiewicz, J., & Wilkes, B. J., 2000, *ApJ*, 542, 692  
 Laor, A., Jannuzi, B. T., Green, R. F., & Boroson, T. A., 1997, *ApJ*, 489, 656  
 Laor, A., 2000, *NewA Rev.*, 44, 503  
 Lawrence, A., 1991, *MNRAS*, 252, 586  
 Leighly, K. M., 1999, *ApJS*, 125, 317  
 Leighly, K. M., 2001, in *ASP Conf. Ser. 224, Probing the Physics of Active Galactic Nuclei*, ed. Peterson, B. M., Pogge, R. W., & Polidan, R. S. (San Francisco: ASP), 293  
 Mathur, S., 2000, *MNRAS*, 314, 17  
 McIntosh, D. H., Rix, H.-W., Rieke, M. J., & Foltz, C. B. 1999, *ApJ*, 517, 73  
 Moran, E. C., Halpern, J. P., & Helfand, D. J., 1996, *ApJS*, 106, 341  
 Murray, N., & Chiang, J., 1998, *ApJ*, 494, 125  
 Nagao, T., Murayama, T., Shioya, Y., & Taniguchi, Y., 2002, *ApJ*, 575, 721  
 Oke, J. B., & Lauer, T. R., 1979 *ApJ*, 230, 360  
 Osmer, P. S., Porter, A. C., & Green, R.F. 1994, *ApJ*, 436, 678  
 Osmer, P. S., & Shields, J. C. 1999, in *ASP Conf. Ser. 162, Quasars and Cosmology*, ed. G. Ferland & J. Baldwin (San Francisco: ASP), 235  
 Osterbrock, D. E. & Pogge, R. W., 1985, *ApJ*, 297, 166  
 Penston, M. V., Fosbury, R. A. E., Boksenberg, A., Ward, M. J., & Wilson, A. S., 1984, *MNRAS*, 208, 347  
 Pounds, K., Done, C., & Osbourne, J., 1995, *MNRAS*, 277, 5  
 Proga, D., Stone, J. M., & Kallman, T. R., 2000, *ApJ*, 543, 686  
 Puchnarewicz, E. M., Mason, K. O., Siemiginowska, A., & Pounds, K. A., 1995, *MNRAS*, 276, 20  
 Rodriguez-Pascual, P. M., Mas-Hesse, J. M., & Santos-Lleo, M., 1997, *A&A*, 327, 72  
 Rodriguez-Pascual, P. M., Pastoriza, M. G., & Donzelli, C. J., 2000, *ApJS*, 126, 63  
 Schlegel, D. J., Finkbeiner, D. P., & Davis, M., 1998, *ApJ*, 500, 525  
 Schneider, D. P., Schmidt, M., & Gunn, J. E., 1991, *AJ*, 101, 2004  
 Schneider, D. P., et al., 2001, *AJ*, 121, 1232S  
 Shang Z., Wills, B. J., Robinson, E. L., Wills, D., Laor, A., Xie, B., & Yuan, J., 2003, *ApJ*, in press  
 Shemmer, O., & Netzer, H. 2002, *ApJ*, 567, 19  
 Shields, J. C., & Hamann, F. 1997, *RevMexAA (Serie de Conf.)*, 6, 221  
 Stirpe, G. M., 1990, *A&AS*, 85, 1049  
 Sulentic, J. W., Marziani, P., Zamanov, R., Bachev, R., Calvani, M., & Dultzin-Hacyan, D., 2002, *ApJ*, 566, 71  
 Telfer, R. C., Zheng, W., Kriss, G. A., & Davidsen, A. F., 2002, *ApJ*, 565, 773  
 Tytler, D., & Fan, X. M. 1992, *ApJS*, 79, 1  
 van Groningen, E., 1993, *A&A*, 272, 25  
 Vanden Berk, D. E., et al., 2001, *AJ*, 122, 549  
 Verner, D. A., Verner, E. M., & Ferland, G. J., 1996, *Atomic Data Nucl. Data Tables*, 64, 1  
 Verner, E. M., Verner, D. A., Korista, K. T., Ferguson, J. W., Hamann, F., & Ferland, G. J., 1999, *ApJS*, 120, 101  
 Véron-Cetty, M. -P., Véron, P., & Gonçalves, A. C., 2001, *A&A*, 372, 730  
 Vestergaard, M., & Wilkes, B. J., 2001, *ApJS*, 134, 1  
 Wang, T., Brinkmann, W., & Bergeron, J., 1996, *A&A*, 309, 81  
 Wills, B. J., Brotherton, M. S., Laor, A., Wills, D., Wilkes, B. J., Ferland, G., & Shang, Z., 1999, in *ASP Conf. Ser. 162, Quasars and Cosmology*, ed. G. Ferland & J. Baldwin, (San Francisco: ASP), 161  
 Wills, B. J., Shang, Z., & Yuan J. M. 2000, *NewA Rev.*, 44, 511  
 Winkler, H., 1992, *MNRAS*, 257, 677  
 Winkler, H., Stirpe, G. M., & Sekiguchi, K., 1992, *A&AS*, 94, 103  
 Zheng, W., Kriss, G. A., Telfer, R. C., Grimes, J. P., & Davidsen, A. F., 1997, *AJ*, 475, 469

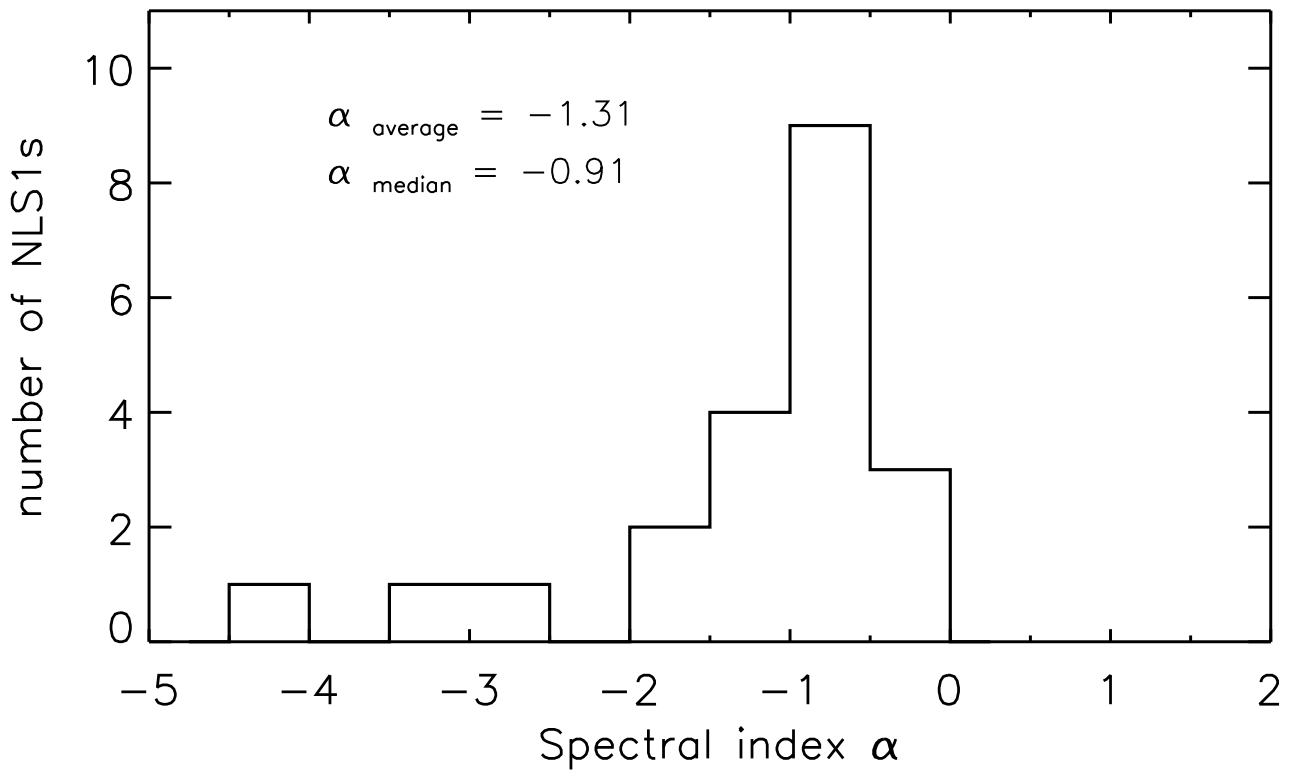


FIG. 1.— Histogram of continuum spectral indices,  $\alpha$ , where  $F_\nu \propto \nu^\alpha$ , for all but one (Mrk110) NLS1 in the sample. The average and median values are indicated.

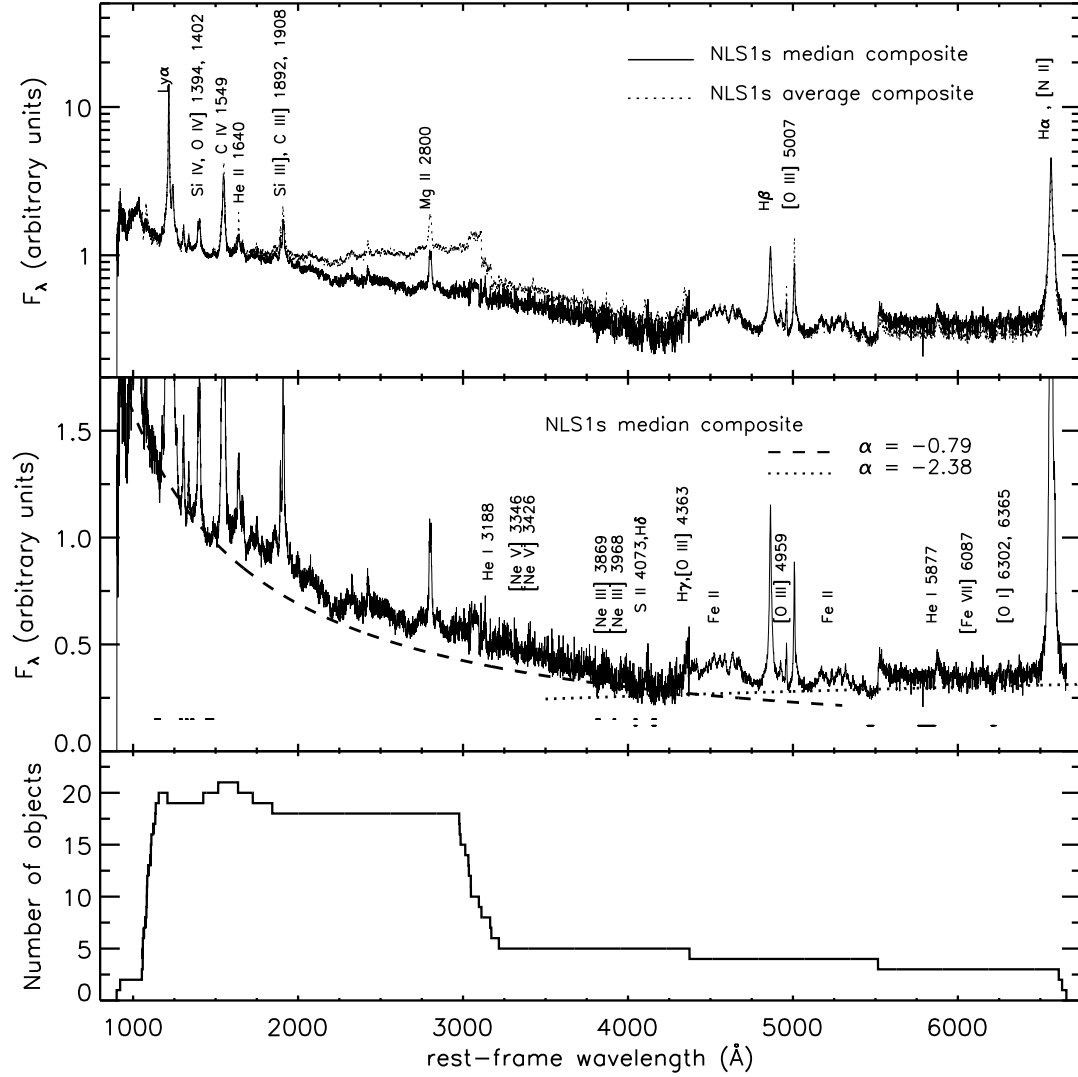


FIG. 2.— *Top panel*: NLS1 composite spectrum plotted as  $\log(F_\lambda)$  vs. rest-frame wavelength, with the principal emission features identified. The flux has been normalized to unit mean flux over the wavelength range 1430 Å–1470 Å. *Middle panel*: The median composite spectrum, plotted on a linear scale, and zoomed near the continuum level for a better visualization of the weak features in the optical range. A more detailed UV line identification is presented in Figure 4. The power-law continuum fits are overplotted as dashed and dotted lines. *Bottom panel*: Number of NLS1s contributing to the composite as a function of rest-frame wavelength.

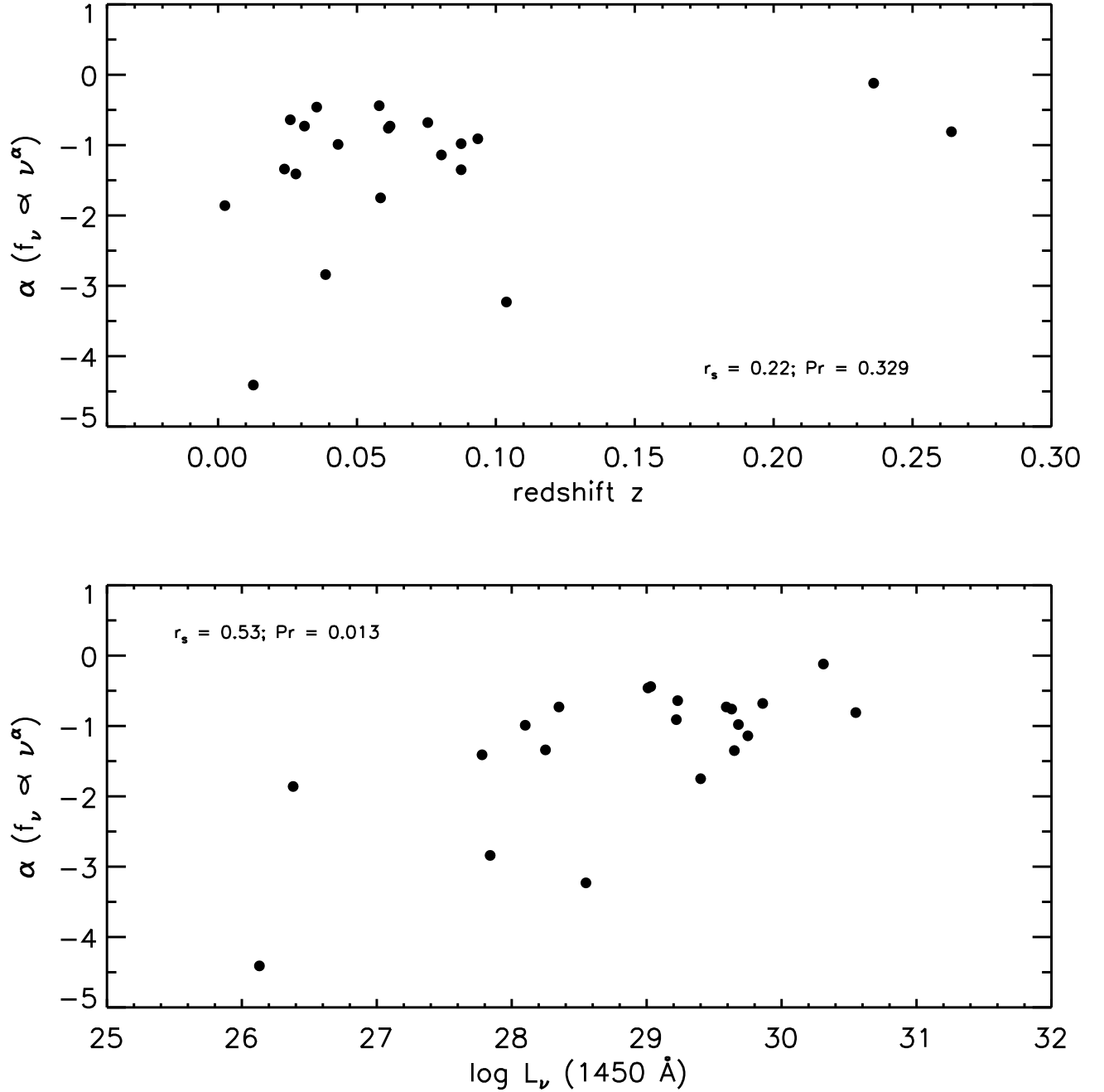


FIG. 3.— Spectral indices plotted vs. redshift (*upper panel*) and 1450Å luminosity (*lower panel*), with  $L_\nu$  expressed in  $\text{ergs s}^{-1} \text{Hz}^{-1}$ . The Spearman rank coefficient and the probability of the correlation happening by chance are indicated. The error bars in both directions are smaller than the symbol size, and therefore not indicated.

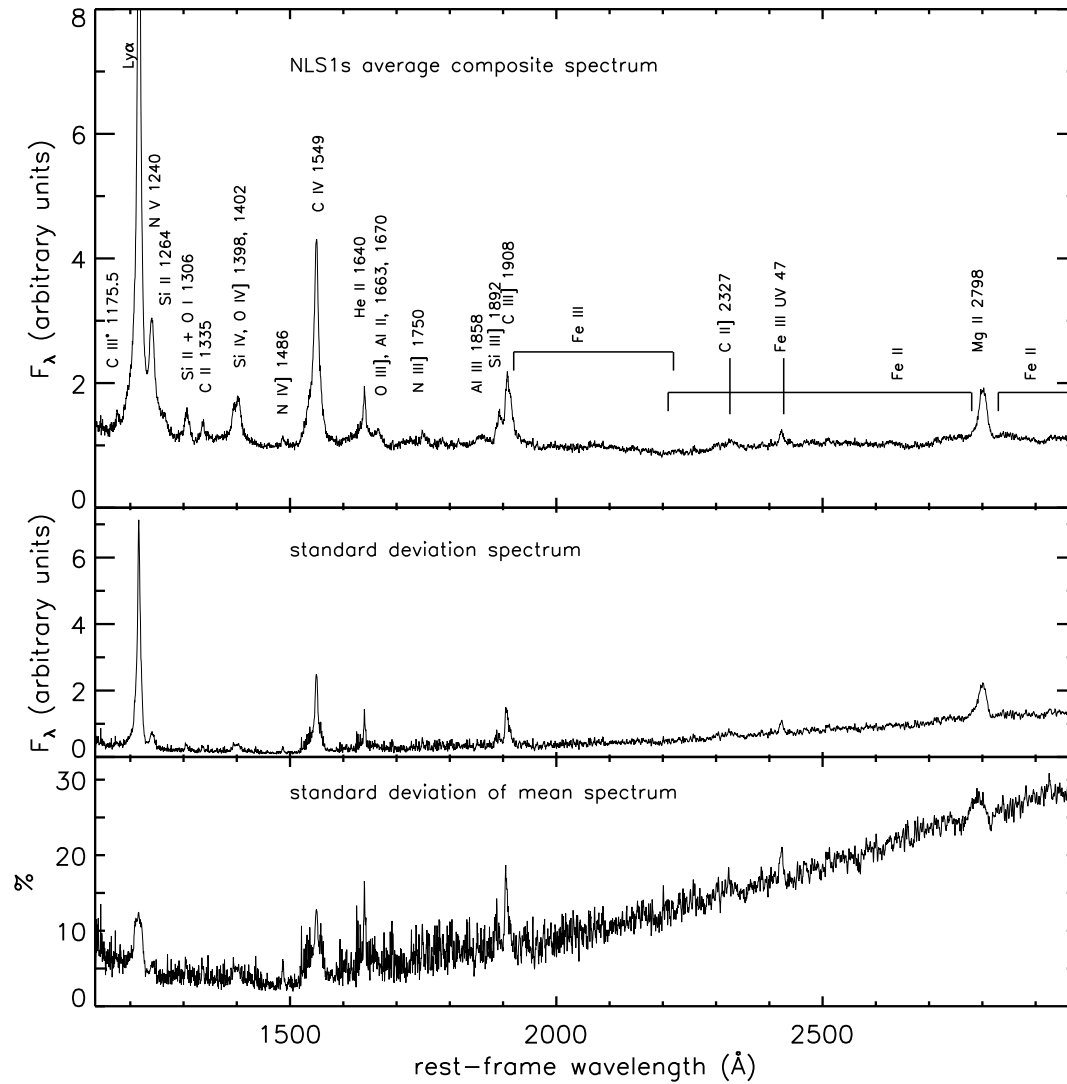


FIG. 4.— *Top panel*: NLS1 average composite spectrum plotted for the UV range only, where at least 18 objects are contributing. The same normalization as in Figure 2 is used. The prominent emission features are marked. *Middle panel*: Flux standard deviation in  $F_\lambda$  relative to the average composite spectrum, as a function of rest-frame wavelength for the individual spectra comprising the composite. *Bottom panel*: The standard deviation of the mean, expressed in percent.

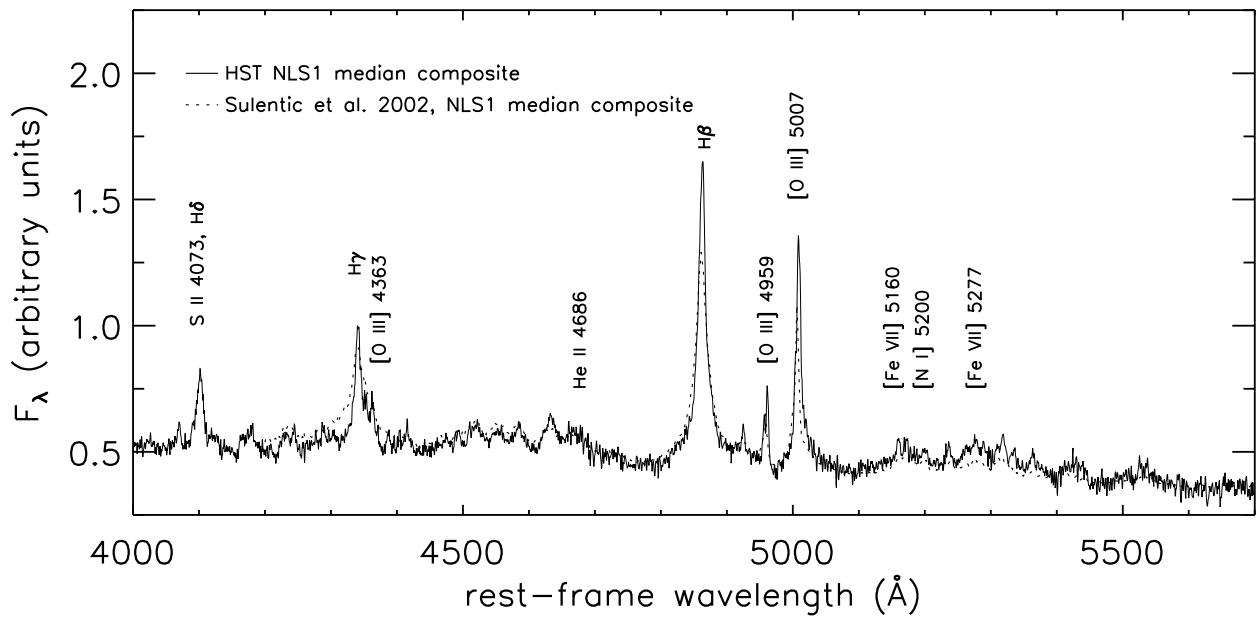


FIG. 5.— The optical range of the *HST* NLS1 median composite, constructed using only the 3 objects that span the whole spectral range. The same flux normalization as in Figure 2 is used. The Sulentic et al. (2002) NLS1 median composite, based on 24 ground-based object spectra, is shown for comparison. The strong similarity between the two medians suggests that the *HST* NLS1 composites are representative of these objects.

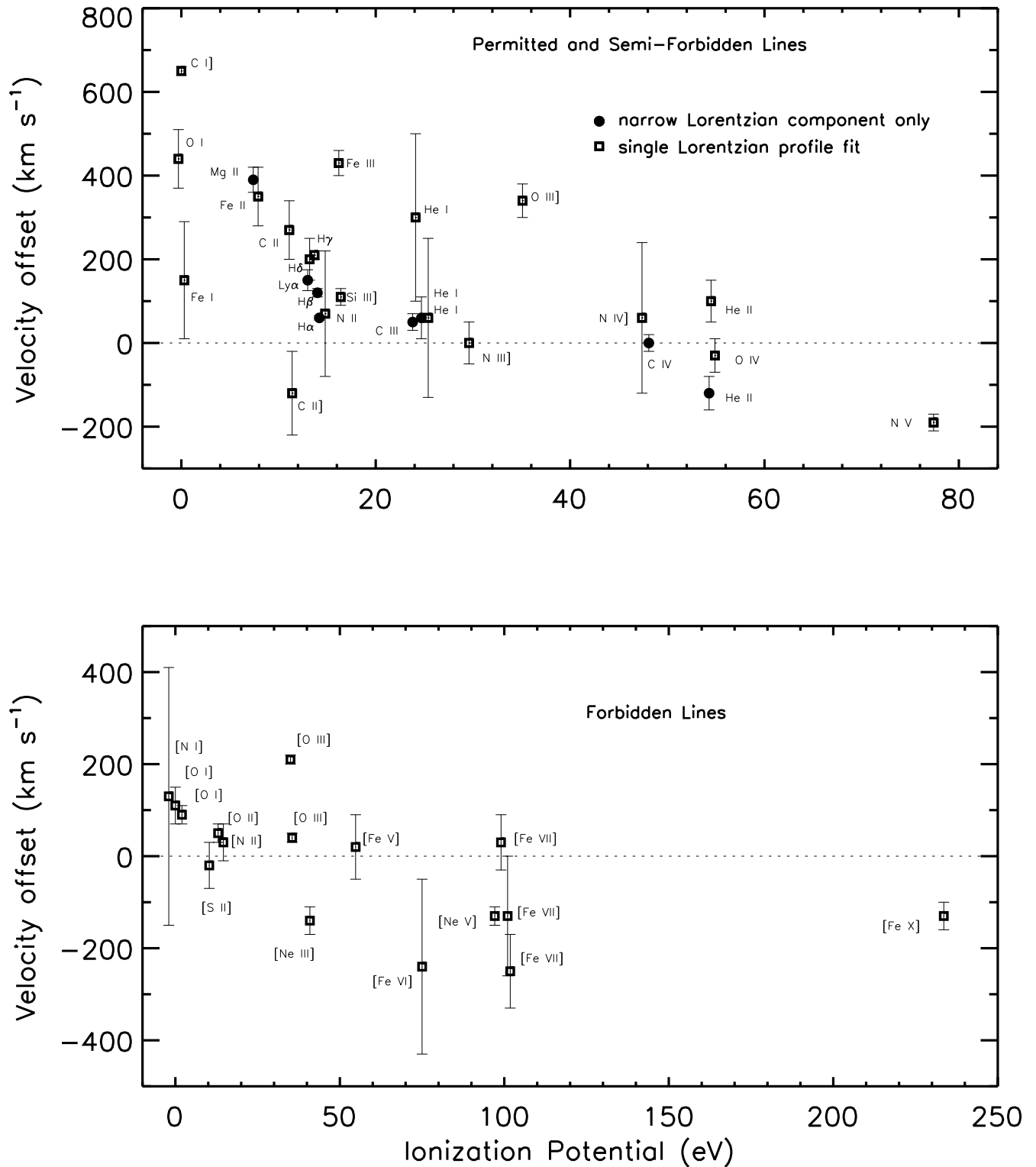


FIG. 6.— Emission-line velocity offsets, relative to the rest frame (defined by C IV $\lambda$ 1549), as a function of ionization potential for selected emission lines (see text). Error bars show the  $1\sigma$  uncertainty in the velocity measurement. Permitted and semi-forbidden lines are shown in the *top panel*, and forbidden lines are shown in the *bottom panel*. Only one measurement is shown for each line, and the point type indicates the adopted profile. Overlapping points are slightly offset horizontally from each other for clarity. The points are labeled by ion.

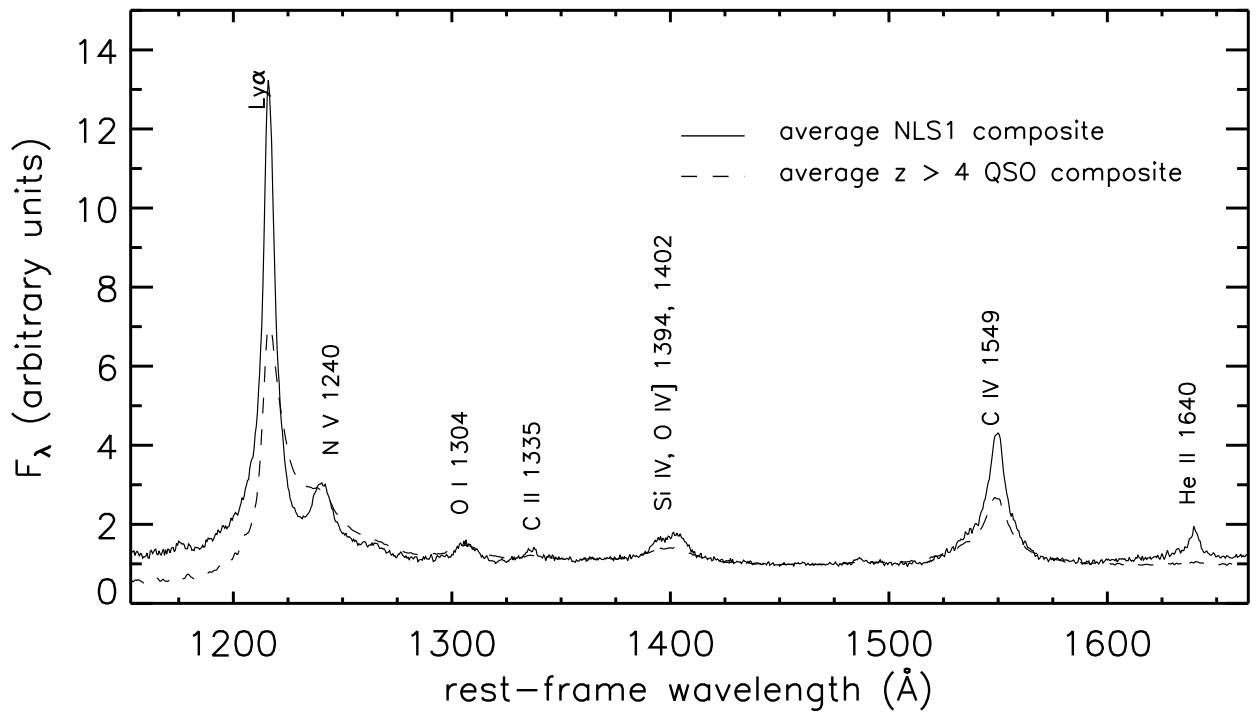


FIG. 7.— Direct comparison between NLS1 and  $z \gtrsim 4$  QSO average composite spectra. The same normalization as in Figure 2 is used.



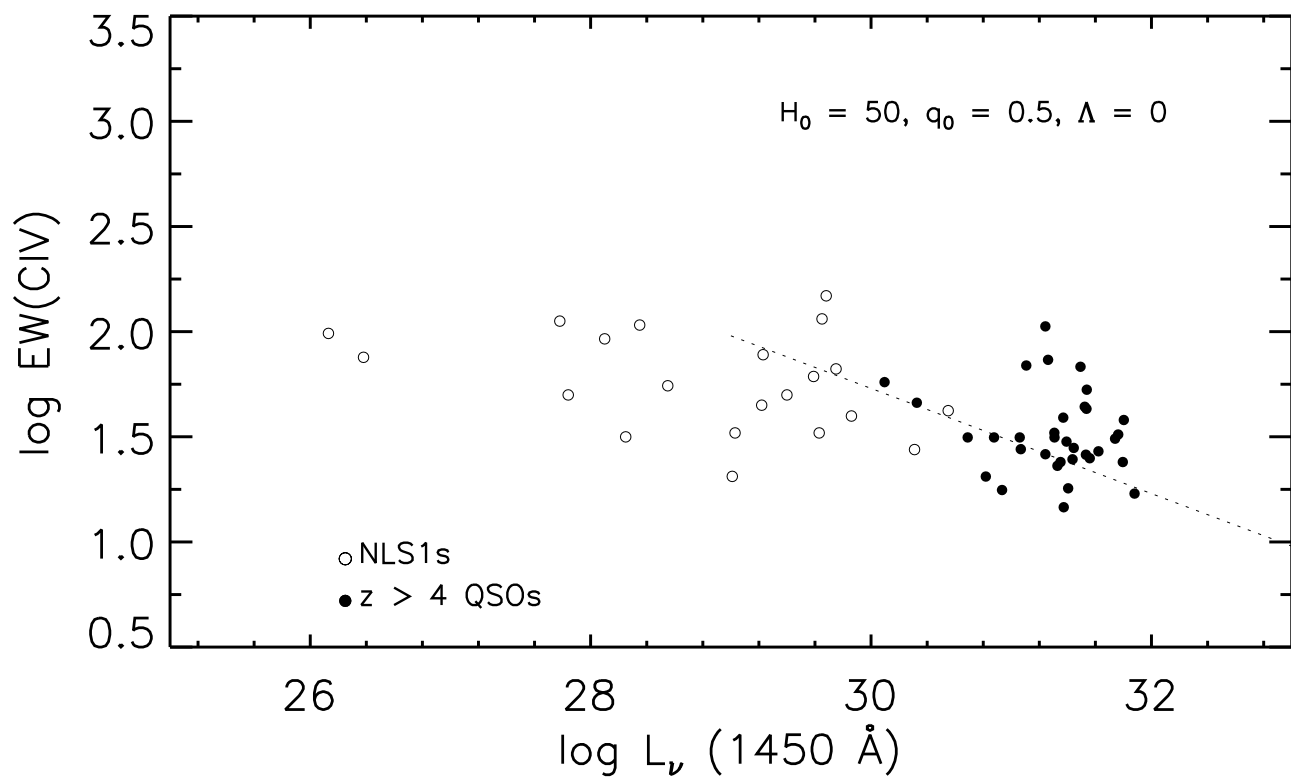


FIG. 8.— Rest-frame EW of the C IV emission line, in  $\text{\AA}$ , as a function of  $1450\text{\AA}$  luminosity, in  $\text{ergs s}^{-1} \text{Hz}^{-1}$ , for individual NLS1 and  $z \gtrsim 4$  QSO spectra. The Baldwin relation found by Osmer, Porter & Green (1994) for a sample of 186 luminous quasars [ $\log L_\nu(1450) \gtrsim 29$ ,  $0 < z < 3.8$ ] is shown as a dotted line.

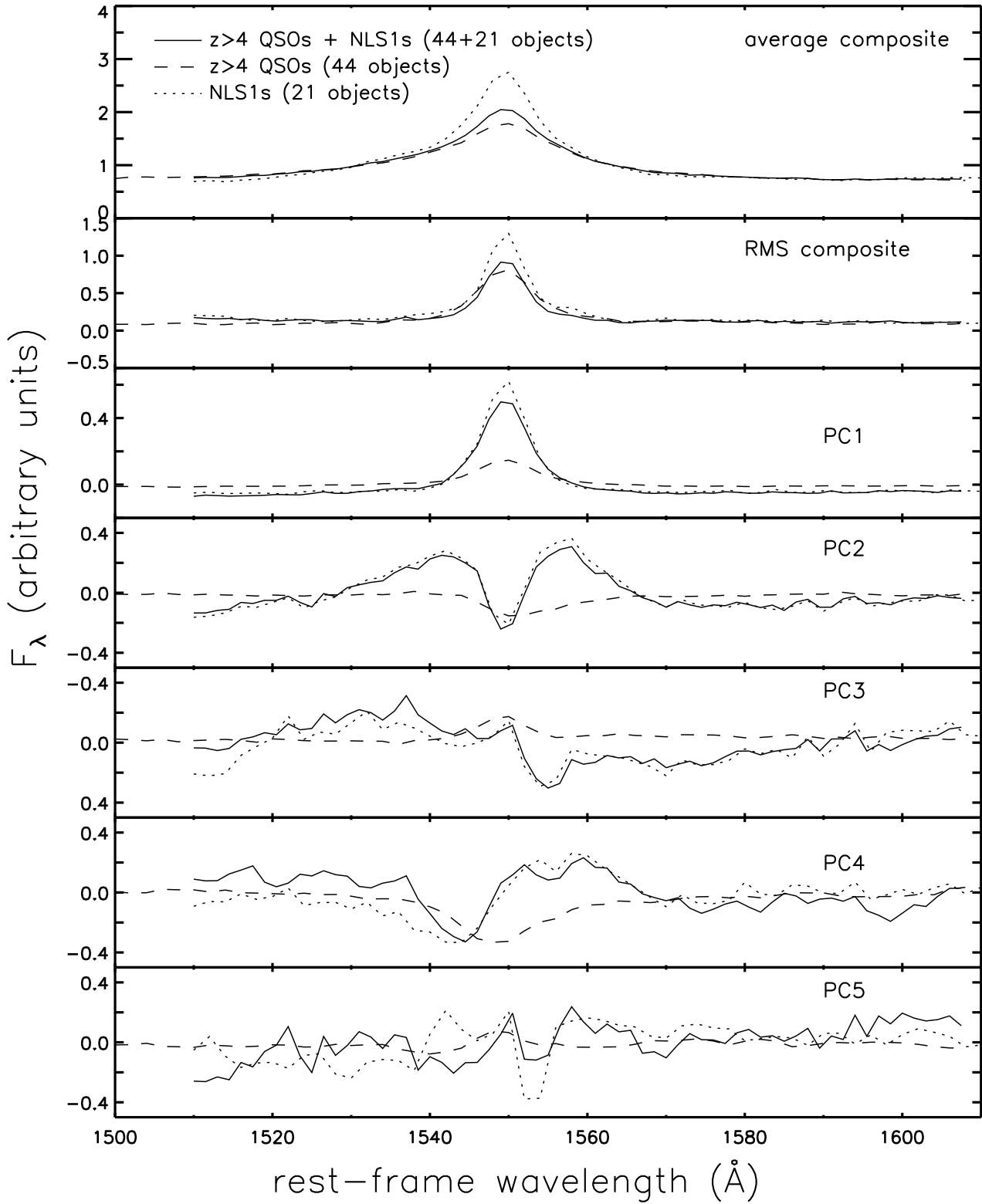


FIG. 9.— Mean and standard deviation spectrum and the first 5 principal components given by PCA, performed for the C IV region only, applied to the NLS1 sample (dotted line), the  $z \gtrsim 4$  QSOs (dashed line), and the combined sample (continuous line). The principal components show similar modulations in the spectral variation in both categories of objects; the amplitude differs.

TABLE 1  
NLS1 SAMPLE

Object	Instr.	Gratings	Coverage <sup>a</sup>	Ref <sup>b</sup>
Ark 564	FOS	G130H,G190H,G270H,G400H,G570H	1087–6817	6,9,10,11
1H0707-495	STIS	G140L,G230L	1122-3155	6
IRAS13224-3809	STIS	G140L,G230L	1117-3148	1,6
IRAS13349+2438	FOS	G190H,G270H	1572-3294	4
KUG 1031+398	FOS	G130H,G190H,G270H	1087-3301	8,11
Mrk110	STIS	G140M	1194-1250	2,11
Mrk335	FOS	G130H,G190H,G270H	1087-3301	2,11
	GHR	G160M	1221-1257	
Mrk478	FOS	G130H,G190H,G270H	1087-3277	2,5,11
	STIS	G140M	1194-1300	
Mrk486	FOS	G190H,G270H	1567-3293	2,11
Mrk493	FOS	G130H,G190H,G270H,G400H,G570H	1087–6817	7,11
Mrk766	STIS	G140L,G230L	1087-3151	3,5,7,11
NGC4051	STIS	E140M	1140-1729	6,11
PG 1211+143	FOS	G130H,G190H,G270H	1087-3275	2,11
	GHR	G140L	1190-1477	
	STIS	G140M	1194-1300	
PG 1351+640	FOS	G130H,G190H,G270H	1087-3301	2
	STIS	G140M	1194-1300	
	STIS	G230L	1568-3151	
PG 1404+226	FOS	G130H,G190H,G270H,G400H	1087-4780	2,11
PG 1411+442	FOS	G130H,G190H,G270H	1087-3276	2
	STIS	G230L	1572-3157	
PG 1444+407	FOS	G130H,G190H	1087-2330	3
RX J0134-42	FOS	G130H,G190H,G270H,G400H,G570H	1087–6817	5
Ton S180	STIS	G140M	1194-1299	5,11,12
	STIS	G140L,G230L	1120-3160	
WPVS007	FOS	G130H,G190H,G270H,G400H,G570H	1087–6817	5,13
I Zw1	FOS	G130H,G190H,G270H	1087-3276	2,11
	FOS	G190H,G270H	1568-3295	
	FOS	G270H	2222-3277	
	GHR	G160M	1221-1257	
II Zw136	STIS	G140M	1194-1300	2
	GHR	G140L	1153-1739	

<sup>a</sup> given in Å

<sup>b</sup>References to optical emission-line measurements that led to their NLS1 classification

References. — (1) Boller et al. (1993); (2) Boroson & Green (1992); (3) Goodrich (1989); (4) Grupe et al. (1998); (5) Grupe et al. (1999); (6) Leighly (1999); (7) Osterbrock & Pogge (1985); (8) Puchnarewicz et al. (1995); (9) Stirpe et al. (1990); (10) van Groningen (1993); (11) Véron-Cetty, Véron & Gonçalves (2001); (12) Winkler (1992); (13) Winkler et al. (1992)

TABLE 2  
NLS1 PROPERTIES

Object	$z^a$	$\log L_\nu(1450)^b$	$\alpha(f_\nu \propto \nu^\alpha)$	EW(C IV) <sup>c</sup>	$\Gamma_{\text{ROSAT}}$	Ref <sup>e</sup>
Ark 564 <sup>d</sup>	0.0239	28.25	-1.34±0.01	31.6	3.4±0.1	1
1H0707-495 <sup>d</sup>	0.0355	29.01	-0.46±0.01	20.5	2.3±0.3	3
IRAS13224-3809	0.0580	29.03	-0.44±0.02	33.0	4.5±0.1	1, 3
IRAS13349+2438	0.1038	28.55	-3.23±0.06	55.3	2.8±0.1	3
KUG 1031+398	0.0432	28.10	-0.99±0.02	92.4	4.3±0.1	1
Mrk110	0.0340	...	...	...	2.4±0.1	4
Mrk335	0.0260	29.23	-0.64±0.01	77.7	2.9±0.1	3
Mrk478	0.0755	29.86	-0.68±0.01	39.7	3.1±0.1	1, 3
Mrk486 <sup>d</sup>	0.0387	27.84	-2.84±0.09	50.0	...	...
Mrk493	0.0311	28.35	-0.73±0.01	107.5	2.7±0.2	1
Mrk766 <sup>d</sup>	0.0127	26.13	-4.41±0.04	98.1	2.7±0.1	1, 3
NGC4051 <sup>d</sup>	0.00245	26.38	-1.86±0.04	75.5	2.8±0.0	3
PG 1211+143	0.0804	29.75	-1.14±0.01	66.5	3.1±0.2	3, 4
PG 1351+640 <sup>d</sup>	0.0875	29.65	-1.35±0.01	115.0	2.5±0.6	4
PG 1404+226 <sup>d</sup>	0.0935	29.22	-0.91±0.01	44.7	4.1±0.2	3, 4
PG 1411+442 <sup>d</sup>	0.0875	29.68	-0.98±0.03	148.0	3.0±0.5	4
PG 1444+407	0.2640	30.55	-0.81±0.04	42.1	...	...
RX J0134-42 <sup>d</sup>	0.2360	30.31	-0.12±0.01	27.5	7.7±2.6	2
Ton S180	0.0613	29.63	-0.76±0.01	33.0	3.0±0.1	3
WPVS007 <sup>d</sup>	0.0280	27.78	-1.41±0.01	112.2	9.0±2.0	2
I Zw1	0.0585	29.40	-1.75±0.01	50.0	3.1±0.1	1, 3
II Zw136	0.0619	29.59	-0.73±0.04	61.2	3.2±...	4

<sup>a</sup> calculated from the observed spectra using the C IV emission-line; the only exception is Mrk110 for which the line is not available, and the redshift is taken from the literature

<sup>b</sup>to ease comparison with earlier published work, an  $H_0 = 50 \text{ km s}^{-1}\text{Mpc}^{-1}$ ,  $q_0 = 0.5$ ,  $\Lambda = 0$  cosmology was adopted. The values reflect flux measurements which are corrected for Galactic extinction; typical uncertainties are  $\sim 0.05$  dex.

<sup>c</sup>rest-frame EWs (in  $\text{\AA}$ ) calculated by fitting a single Lorentzian profile to the line

<sup>d</sup>Emission lines are contaminated by absorption; indicated measurements (EWs), obtained from the polynomial interpolated profiles, should be regarded as lower limits

<sup>e</sup>References for the  $\Gamma_{\text{ROSAT}}$  values

References. — (1) Boller, Brandt & Fink (1996); (2) Grupe et al. (1998); (3) Leighly (1999); (4) Wang et al. (1996)

TABLE 3  
EMISSION-LINE MEASUREMENTS

Line <sup>a</sup>	$\lambda_{lab}^c$ (Å)	$\lambda_{mean\_rest}^d$ (Å)	$\Delta v$ (km s <sup>-1</sup> )	Rel. Flux <sup>f</sup> [100 × F/F(Ly $\alpha$ )]	EW <sup>g</sup> (Å)	FWHM <sup>h</sup> (km s <sup>-1</sup> )
C III*	1175.5	1175.5±0.5	0±130	0.9±0.2	1.1	1190± 690
Si II	1197.4	1199.3±0.7	480±170	0.5±0.2	0.6	790± 500
Si III	1206.5	1206.7±1.9	50±470	0.4±0.6	0.5	780±1350
Ly $\alpha$	1215.7	...	...	100.0±1.6	131.8	...
..narrow	1215.7	1216.3±0.1	150±25	69.5±0.9	91.6	1480± 10
..broad	1215.7	1212.6±1.4	-760±340	30.6±1.0	40.2	7000± 280
N V	1240.8	1240.0±0.1	-190±20	13.0±1.5	17.6	2110± 130
Si II*	1248.4	1245.0±0.4	-810±90	3.7±1.0	5.0	2200± 400
Si II	1264.8	1262.9±0.9	-450±210	3.5±0.4	4.8	3510± 350
O I	1303.5	1305.4±0.3	440±70	3.7±0.6	5.5	2060± 130
Si II	1309.3	1309.1±1.5	-40±340	1.0±0.7	1.5	2030± 280
C II	1335.3	1336.5±0.3	270±70	2.6±0.3	4.0	1930± 260
N II <sup>b</sup>	1344.6	1349.0±0.9	980±200	1.1±0.3	1.7	2020± 430
Si IV+O IV]	1400.0	...	...	10.5±3.2	17.2	...
..Si IV	1393.7	1393.7±0.7	0±150	3.1±2.2	5.1	1520± 600
..O IV]	1401.4	1404.6±1.5	680±320	5.4±2.3	8.9	2030± 440
..Si IV	1402.7	1399.9±2.7	-590±570	2.0±0.7	3.3	1520± 690
N IV]	1486.5	1486.8±0.9	60±180	0.7±0.3	1.2	2020±1910
Si II	1530.1	1536.9±0.2	1330±40	4.6±0.8	7.9	2030± 280
C IV	1549.5	...	...	44.8±1.7	77.1	...
..narrow	1549.5	1549.5±0.1	0±20	33.3±1.3	57.3	1900± 60
..broad	1549.5	1541.6±8.2	-1520±1580	11.5±1.1	19.8	12000±2500
He II	1640.4	...	...	23.3±2.6	41.5	...
..narrow	1640.4	1639.7±0.2	-120±40	6.4±0.8	11.4	1780± 240
..broad	1640.4	1630.4±3.0	-1820±540	16.9±2.5	30.1	11990±4090
O III]	1663.5	1665.4±0.2	340±40	4.1±1.1	6.2	2500± 480
Al II	1670.8	1680.0±1.5	1650±260	1.3±1.0	1.9	2250±1330
N II	1725.2	1725.6±0.9	70±150	2.2±0.9	3.3	4710±2100
N III]	1750.5	1750.5±0.3	0±50	2.0±0.2	3.0	1480± 170
Fe II UV191	1785.4	1785.3±0.7	-20±110	1.2±0.2	1.8	1430± 250
Si II	1814.1	1816.9±0.5	460±80	0.6±0.2	0.9	1250± 730
Al III	1858.8	1853.5±1.1	-850±170	1.3±0.5	1.9	2240± 540
Fe III UV52	1867.9	1864.1±0.8	-610±120	1.7±0.5	2.6	2760± 730
Si III]	1892.0	1892.7±0.1	110±20	3.6±0.5	5.5	1250± 130
C III	1907.9	...	...	21.1±5.7	32.2	...
..narrow	1907.9	1908.2±0.1	50±20	10.0±0.6	15.3	1380± 10
..broad	1907.9	1907.7±4.6	-30±720	11.0±5.7	16.9	12230±1110
N II]	2141.4	2144.0±0.9	360±130	0.3±0.2	0.4	1040±1140
C II]	2327.5	2326.6±0.8	-120±100	3.7±1.3	5.7	2540±430
Fe III UV 47	2419.3	2422.8±0.2	430±30	3.2±0.5	5.1	1560±200
O II	2438.8	2439.3±0.6	60±70	0.7±0.2	1.2	1060±250
[O II]	2470.9	2467.6±0.8	-400±100	0.9±0.3	1.5	1570±470
C I] <sup>b</sup>	2478.6	2484.0±0.1	650±10	2.3±0.6	3.7	2580±510
Al II]	2669.9	2674.7±0.4	540±50	0.8±0.6	1.3	1050±430
Mg II	2797.9	...	...	31.4±6.6	58.0	...
..narrow	2797.9	2801.6±0.3	390±30	11.2±2.2	20.7	1680±60
..broad	2797.9	2798.3±0.4	40±40	20.2±6.5	37.4	4620±1090
O III <sup>e</sup>	2960.6	2957.4±1.7	-320±170	0.3±0.2	0.9	850±600
Fe II <sup>e</sup>	2964.3	2966.7±3.6	240±360	0.1±0.1	0.2	830±900
O IV <sup>e</sup>	2982.5	2981.9±2.5	-60±250	0.3±0.3	0.9	820±610
Ne III] <sup>e</sup>	2986.9	2990.0±0.1	310±10	0.2±0.1	0.5	830±680
F V <sup>e</sup>	3109.0	3109.5±0.4	50±40	0.6±0.1	2.0	550±10

TABLE 3—*Continued*

Line <sup>a</sup>	$\lambda_{lab}^c$ (Å)	$\lambda_{mean\_rest}^d$ (Å)	$\Delta v$ (km s <sup>-1</sup> )	Rel. Flux <sup>f</sup> [100 × F/F(Ly $\alpha$ )]	EW <sup>g</sup> (Å)	FWHM <sup>h</sup> (km s <sup>-1</sup> )
O III <sup>e</sup>	3122.5	3122.9±1.3	40±120	0.8±0.4	2.7	910±370
O III <sup>e</sup>	3133.7	3134.2±1.3	50±120	1.8±0.4	6.0	940±210
C II <sup>e</sup>	3166.7	3165.3±0.6	-130±60	0.8±0.3	2.7	760±390
He I	3188.6	3190.6±1.7	190±160	0.7±0.1	1.6	990±230
O IV <sup>b</sup>	3216.8	3215.7±0.5	-100±50	0.5±0.1	1.1	830±120
Ne II <sup>b</sup>	3230.6	3230.9±0.8	30±70	0.9±0.2	2.1	940±260
Fe I Opt91	3261.2	3260.8±0.7	-40±60	1.0±0.1	2.5	840±130
Fe II Opt1	3281.2	3281.6±0.5	40±40	1.2±0.1	3.0	840±70
[Fe III] <sup>b</sup>	3308.5	3307.8±2.4	-60±220	0.7±0.1	1.9	830±110
[Ne V]	3346.8	3345.3±0.2	-130±20	0.5±0.3	1.2	790±260
[Ne V]	3426.8	3425.3±0.2	-130±20	1.2±0.3	3.3	790±260
Fe II <sup>b</sup>	3495.6	3496.2±0.5	50±40	1.5±0.1	4.4	880±100
[Fe VII]	3587.1	3584.1±1.0	-250±80	0.6±0.3	1.8	1080±180
O II <sup>b</sup>	3621.0	3620.6±1.0	-30±80	0.6±0.1	1.8	1280±310
N III <sup>b</sup>	3685.9	3686.3±0.8	30±60	0.5±0.3	1.5	1170±110
[O II]	3727.1	3727.7±0.2	50±20	1.0±0.1	3.3	610±70
[O II]	3729.8	3730.3±0.2	50±20	0.1±0.1	0.2	610±70
[Ne II]	3745.7	3749.0±0.1	290±20	0.4±0.1	1.0	870±250
[Fe VII]	3759.7	3758.3±0.6	-110±60	0.5±0.2	1.4	790±350
[Fe IV]	3769.7	3769.4±1.2	-30±100	0.3±0.1	1.1	790±140
Fe I	3785.3	3787.2±1.8	150±140	1.7±0.1	5.6	3620±190
[Ne III]	3870.1	3868.3±0.3	-140±20	1.1±0.1	4.0	680±190
He I	3889.7	3890.5±2.5	60±190	0.7±0.2	2.6	920± 410
O III]	3938.7	3939.2±1.0	40±70	0.4±0.1	1.5	830±190
[Ne III]	3968.9	3966.9±0.3	-150±20	0.3±0.1	1.2	660±190
O II <sup>b</sup>	3969.6	3971.3±0.5	130±40	1.1±0.1	4.0	830±70
[S II]	4069.7	4069.5±0.8	-20±60	0.2±0.1	0.8	600±270
[S II]	4077.5	4077.3±0.7	-20±50	0.1±0.1	0.3	600±260
H $\delta$	4102.9	4105.6±0.7	200±50	3.7±0.1	14.9	2240±160
Fe III <sup>b</sup>	4180.0	4181.7±0.8	120±60	1.4±0.1	5.8	1220±220
Fe II	4234.3	4239.2±1.0	350±70	1.3±0.1	5.7	1010±150
H $\gamma$	4341.6	4344.7±0.2	210±10	7.3±0.2	26.3	1070±50
[O III]	4364.4	4367.4±0.1	210±10	0.7±0.1	2.4	270±60
He I <sup>b</sup>	4472.7	4477.2±3.1	300±200	0.6±0.2	2.2	1270±280
He II	4687.0	4688.6±0.9	100±50	4.9±0.1	19.0	2890±80
H $\beta$	4862.6	...	...	20.5±1.1	81.5	...
..narrow	4862.6	4864.6±0.1	120±10	17.5±0.3	69.6	1020±10
..broad	4862.6	4864.5±9.9	120±610	3.0±1.1	11.9	6890±200
[O III]	4960.2	4963.4±0.1	40±10	2.3±0.1	9.0	260±10
[O III]	5008.2	5008.5±0.1	40±10	8.0±0.2	31.3	260±10
[Fe VII]	5159.8	5162.1±1.4	-130±130	0.9±0.3	3.8	1080±150
[Fe VI]	5177.5	5180.2±1.9	-240±190	1.2±0.3	4.8	860±250
[N I]	5200.5	5203.5±2.9	130±280	0.8±0.8	3.3	870±820
[Fe VII]	5277.3	5278.3±1.4	-130±130	1.8±0.3	7.4	1080±150
O IV <sup>b</sup>	5318.7	5318.2±0.7	-30±40	1.3±0.2	5.3	750±120
He I	5877.3	...	...	2.3±0.1	11.1	...
..narrow	5877.3	5878.4±1.1	60±50	1.5±0.1	7.5	970±70
..broad	5877.3	5881.4±9.1	210±460	0.7±0.1	3.6	5010±550
[Fe VII]	6087.9	6088.5±1.3	30±60	0.3±0.5	1.4	870±340
[Fe V]	6088.5	6088.8±1.5	20±70	0.4±0.6	2.0	870±290
[O I]	6302.1	6304.5±0.8	110±40	1.2±0.1	6.4	1150±150
[O I]	6365.5	6367.5±0.5	90±20	0.4±0.1	2.2	1140±150

TABLE 3—*Continued*

Line <sup>a</sup>	$\lambda_{lab}$ <sup>c</sup> (Å)	$\lambda_{mean\_rest}$ <sup>d</sup> (Å)	$\Delta v$ (km s <sup>-1</sup> )	Rel. Flux <sup>f</sup> [100 × F/F(Ly $\alpha$ )]	EW <sup>g</sup> (Å)	FWHM <sup>h</sup> (km s <sup>-1</sup> )
[Fe X]	6376.3	6373.5±0.6	-130±30	1.2±0.1	6.5	810±90
[N II]	6548.8	6549.5±0.9	30±40	1.8±0.6	10.1	760±70
H $\alpha$	6564.6	...	...	61.0±1.4	344.2	...
..narrow	6564.6	6565.9±0.1	60±5	57.8±1.0	325.8	760±20
..broad	6564.6	6566.7±0.4	90±20	3.3±1.2	18.4	5500±1140
[N II]	6585.3	6585.9±0.9	30±40	6.1±0.6	34.3	760±70

<sup>a</sup>Emission lines are measured from the average composite spectrum unless otherwise noted

<sup>b</sup>Uncertain identifications

<sup>c</sup>vacuum wavelengths, both below and above 2200Å

<sup>d</sup>given by the centroid of the Lorentzian fit

<sup>f</sup>The line fluxes are normalized to the Ly $\alpha$  flux to ease comparison with published results for other AGN/quasar samples

<sup>e</sup>Lines measured from the median composite

<sup>g</sup>The errors in EWs are not quoted as the relative errors are the same as for the fluxes

<sup>h</sup>Intrinsic width of the emission line; an instrumental broadening of 230 km s<sup>-1</sup>, the approximate FOS spectral resolution, high-resolution gratings, was assumed

TABLE 4  
PROPORTIONS OF PCs IN THE C IV EMISSION REGION

Component	NLS1 (21 obj.)	$z \gtrsim 4$ QSO (44 obj.)	Combined sample (65 obj.)
PC1	0.358	0.272	0.296
PC2	0.139	0.077	0.091
PC3	0.097	0.071	0.061
PC4	0.064	0.053	0.051
PC5	0.046	0.044	0.041